Journal of Computational Physics 229 (2010) 5755–5787

Contents lists available at ScienceDirect

Journal of Computational Physics

journal homepage: www.elsevier.com/locate/jcp

A two-dimensional unstructured cell-centered multi-material ALE scheme using VOF interface reconstruction

Stéphane Galera [b], Pierre-Henri Maire [a,*], Jérôme Breil [b]

[a] CEA CESTA/DSGA, BP 2, 33 114 Le Barp, France
[b] UMR CELIA, Université Bordeaux I 351, Cours de la Libération, 33 405 Talence, France

ARTICLE INFO

Article history:
Received 1 February 2010
Received in revised form 4 April 2010
Accepted 10 April 2010
Available online 20 April 2010

Keywords:
Lagrangian hydrodynamics
Cell-centered scheme
Godunov-type method
Compressible flow
High-order finite volume methods
Multi-dimensional unstructured mesh
Arbitrary Lagrangian–Eulerian methodology
Interface reconstruction

ABSTRACT

We present a new cell-centered multi-material arbitrary Lagrangian–Eulerian (ALE) scheme to solve the compressible gas dynamics equations on two-dimensional unstructured grid. Our ALE method is of the explicit time-marching Lagrange plus remap type. Namely, it involves the following three phases: a Lagrangian phase wherein the flow is advanced using a cell-centered scheme; a rezone phase in which the nodes of the computational grid are moved to more optimal positions; a cell-centered remap phase which consists of interpolating conservatively the Lagrangian solution onto the rezoned grid. The multi-material modeling utilizes either concentration equations for miscible fluids or the Volume Of Fluid (VOF) capability with interface reconstruction for immiscible fluids. The main original feature of this ALE scheme lies in the introduction of a new mesh relaxation procedure which keeps the rezoned grid as close as possible to the Lagrangian one. In this formalism, the rezoned grid is defined as a convex combination between the Lagrangian grid and the grid resulting from condition number smoothing. This convex combination is constructed through the use of a scalar parameter which is a scalar function of the invariants of the Cauchy–Green tensor over the Lagrangian phase. Regarding the cell-centered remap phase, we employ two classical methods based on a partition of the rezoned cell in terms of its overlap with the Lagrangian cells. The first one is a simplified swept face-based method whereas the second one is a cell-intersection-based method. Our multi-material ALE methodology is assessed through several demanding two-dimensional tests. The corresponding numerical results provide a clear evidence of the robustness and the accuracy of this new scheme.

1. Introduction

Numerical schemes in compressible fluid dynamics make use of two classical kinematic descriptions: the Lagrangian description and the Eulerian description. Lagrangian algorithms are characterized by computational cells that move with fluid velocity. They allow an easy and natural tracking of free surfaces and interfaces between different materials. However, they suffer from a lack of robustness when they are facing large flow distortions. On the other hand, Eulerian algorithms are characterized by a fixed computational grid through which fluid moves. They can handle large distortions without any difficulties. However, the numerical diffusion inherent in advection terms discretization leads to an inaccurate interface definition and a loss in the resolution of flow details. The arbitrary Lagrangian–Eulerian (ALE) description has been initially introduced in the seminal paper [22] to solve in a certain extent the shortcomings of purely Lagrangian and purely Eulerian

* Corresponding author.
E-mail address: maire@celia.u-bordeaux1.fr (P.-H. Maire).

0021-9991/$ - see front matter © 2010 Elsevier Inc. All rights reserved.
doi:10.1016/j.jcp.2010.04.019

descriptions by combining the best features of both aforementioned approaches. The main feature of the ALE methodology is to move the computational grid with a prescribed velocity field to improve the accuracy and the robustness of the simulation. ALE methods have been used for several decades to face successfully the difficulties inherent in the simulation of multi-material fluid flows with large distortions [3,5,43,23,8,15,39,13]. Usually, ALE methods can be implemented in two manners. The first one, which is termed direct ALE, consists in an unsplit moving mesh discretization of the gas dynamics equations wherein the grid velocity is typically deduced from boundaries motion [44,36]. In this approach convective terms are solved directly. The second one, which is the subject of the present paper, is named indirect ALE. The main elements of an indirect ALE approach are an explicit Lagrangian phase in which the physical variables and grid are updated, a rezoning phase in which nodes of the Lagrangian grid are moved to improve the geometric quality of the grid and a remapping phase wherein the physical variables are conservatively interpolated from the Lagrangian grid onto the new rezoned one [40]. We point out that indirect ALE method encompasses both Lagrangian and Euler approaches. Indeed, when the rezoned mesh coincides with the initial mesh, indirect ALE algorithm corresponds to an Eulerian algorithm which is termed as Lagrange plus remap algorithm wherein advection terms are solved through the use of the remapping phase.

This paper aims at presenting a cell-centered indirect ALE algorithm to solve multi-material compressible flows on two-dimensional unstructured grids with fixed topology. Our Lagrangian phase solves the gas dynamics equations utilizing a moving mesh cell-centered discretization wherein the physical conservation laws are discretized in a compatible manner with the nodal velocity so that the geometric conservation law (GCL) is exactly satisfied [13]. Namely, the time rate of change of a Lagrangian volume is computed consistently with the node motion. This critical requirement is the cornerstone of any Lagrangian multidimensional scheme. Nowadays, cell-centered finite volume schemes [12,38,37] that fulfill this GCL requirement seem to be a promising alternative to the usual staggered finite difference discretization [11]. Moreover, these cell-centered schemes allow straightforward implementation of conservative remapping methods when they are used in the context of ALE. Here, we are using the high-order cell-centered Lagrangian scheme that has been described in [37]. Let us recall that the numerical fluxes are determined by means of a node-centered approximate Riemann solver. This discretization leads to a conservative and entropy consistent scheme whose high-order extension is derived through the use of generalized Riemann problem [7,37].

The thermodynamical modeling of multi-material flows in our ALE algorithm is considered through the use of two different approaches. In the first one, the multi-material flow is viewed as a multi-component mixture of miscible fluids wherein each fluid is characterized by its mass fraction, i.e. concentration. In this modeling, concentration stands for a passive scalar which allows to track the location of each material inside the flow. The mixture equation of state is obtained using a pressure–temperature equilibrium assumption. This modeling is quite simple to implement and to use. However, it can lead to inaccurate results as the numerical diffusion inherent in the concentration remapping may involve spurious numerical mixing. To correct this potential flaw, we have developed another approach which corresponds to the case of immiscible fluids. This second approach is based on the Volume Of Fluid (VOF) methodology which allows a Lagrangian tracking capability for material interfaces. Namely, contrary to concentration equations modeling, there is no mass flux between materials. The VOF approach introduces mixed or multi-material cells, which contain more than one material. Each material is characterized by its volume fraction, i.e. the ratio between the volume occupied by the material and the total volume of the mixed cell. We note that our implementation is restricted to two materials. The main issue related to mixed cell is define its evolution during the Lagrangian phase. To this end, we use a closure model that enables us to compute an effective thermodynamic state in terms of the thermodynamic states of each material and its related volume fraction. Here, we use the classical equal strain model [8], knowing that more sophisticated modeling are possible [4,24]. Knowing the volume fractions field, we perform a reconstruction of the interface in each cell by means of a piecewise linear representation which is obtained extending the well-known Youngs [51] algorithm to unstructured grids.

Essential for successful application of our ALE algorithm is the use of a good mesh rezoning strategy. This is not a simple task, since one has to balance between various requirements, some of which might seem to be contradictory. Generally, a proper rezoning strategy should maintain reasonable geometrical quality of the mesh while respecting the features of the underlying flow imprinted into the mesh deformation during the Lagrangian phase [28]. Since the objectives of mesh rezoning are close to the objectives of mesh generation, the rezoning strategies for ALE are closely related to the techniques developed and used by the mesh generation community. Here, we will restrict ourselves to rezoning by node repositioning, without changing the mesh connectivity. We point out that an original rezoning strategy has recently been developed where the connectivity of the mesh is allowed to change through the use of Voronoi tessellation. This new approach provides a Reconnection-based arbitrary Lagrangian–Eulerian (ReALE) strategy [34,35]. In the context of fixed topology, the geometric rezoning can easily be expressed as an optimization problem, where some mesh quality functional is minimized in order to find suitable mapping from the logical (computational) to the physical (real) space. Typically the functional contains information about smoothness of the mesh, its orthogonality, etc. A classical approach was originally proposed by Winslow [49,50] and is still considered to be the standard method. Here, we are making use of the condition number smoothness functional introduced in [30,29], which is closely related to Winslow smoothing, and is widely used on triangular and structured quadrilateral meshes. A generalized approach will be given, which can be applied to any unstructured meshes. An original relaxation procedure allows to define the rezoned grid as a convex combination between the Lagrangian grid and the regularized grid, i.e. the grid produced by the condition number smoothing. This convex combination is constructed through the use of an ω factor which is expressed in terms of the invariants of the right Cauchy–Green tensor [9] with respect to the Lagrangian displacement over a time

step. This relaxation procedure is Galilean invariant and allows to keep the rezoned grid as close as possible to the Lagrangian grid.

Finally, we are dealing with remapping methods based on a partition of the volume of the rezoned cell in terms of its overlap with the Lagrangian cells. Following the methodology derived in [41] we have developed two approaches for the remapping phase. The first one is a simplified face-based method wherein the volume integral over a new cell is expressed as the volume integral over the old cell plus a sum of surface integrals over the region swept by the displacement of the cell faces from their old to their new locations. This method is quite inexpensive since it does not require finding intersections between old and new cells. However, its use is restricted to grids that have the same connectivity. Thus, it is utilized for ALE computation wherein the multi-material modeling is performed using concentration equations. We note that an extension of this method to polygonal grids with connectivity changing in a Voronoi-like manner has been recently developed [32]. The second approach is the cell-intersection-based method. For a given rezoned cell, its overlap with the Lagrangian cells is exactly calculated. This method is more expensive since it requires finding all intersections between the cells of old and new grids. However, it can handle grids that have completely different connectivity. It is extensively employed in the case of ALE computation wherein the multi-material modeling is based on interface reconstruction. Since in this case, due to the mixed cells occurrence, the rezoned grid and the Lagrangian grid do not share the same topology in the vicinity of the interface.

The paper is structured as follows. Our ALE strategy is presented in Section 2 by describing the flowchart of our multi-material ALE algorithm. For sake of completeness, we recall in Section 3 the main features of our compatible cell-centered Lagrangian discretization. In Section 4, we develop the two approaches (concentration equations and VOF) used to deal with thermodynamical closure in case of multi-material flow. Next, we briefly describe in Section 5 the interface reconstruction method utilized in VOF modeling. Section 6 is devoted to a detailed description of our rezoning and grid relaxation strategies. The conservative interpolation methods used to transfer the physical variables from the Lagrangian grid onto the rezoned one are explained in Section 7. Extensive numerical experiments are reported in Section 8. They demonstrate not only the robustness and the accuracy of the present methodology but also its ability to handle successfully complex two-dimensional multi-material fluid flows computed on unstructured grids. Finally concluding remarks and perspectives about future works are given in Section 9.

2. Arbitrary Lagrangian–Eulerian methodology

2.1. Governing equations

Let $\mathcal{D}$ be a region of the two-dimensional space $\mathbb{R}^2$, filled with an inviscid fluid and equipped with an orthonormal frame. It is convenient, from the point of view of subsequent discretization, to write the unsteady compressible Euler equations in the control volume formulation which holds for an arbitrary moving control volume:

$$\frac{\mathrm{d}}{\mathrm{d}t}\int_{V(t)} \mathrm{d}V - \int_{S(t)} \boldsymbol{U}_g \cdot \boldsymbol{N}\,\mathrm{d}S = 0, \tag{1a}$$

$$\frac{\mathrm{d}}{\mathrm{d}t}\int_{V(t)} \rho\,\mathrm{d}V + \int_{S(t)} \rho(\boldsymbol{U}-\boldsymbol{U}_g)\cdot \boldsymbol{N}\,\mathrm{d}S = 0, \tag{1b}$$

$$\frac{\mathrm{d}}{\mathrm{d}t}\int_{V(t)} \rho\boldsymbol{U}\,\mathrm{d}V + \int_{S(t)} [(\boldsymbol{U}-\boldsymbol{U}_g)\cdot \boldsymbol{N}\rho\boldsymbol{U} + P\boldsymbol{N}]\mathrm{d}S = \boldsymbol{0}, \tag{1c}$$

$$\frac{\mathrm{d}}{\mathrm{d}t}\int_{V(t)} \rho E\,\mathrm{d}V + \int_{S(t)} [(\boldsymbol{U}-\boldsymbol{U}_g)\cdot \boldsymbol{N}\rho E + P\boldsymbol{U}\cdot \boldsymbol{N}]\mathrm{d}S = 0. \tag{1d}$$

Here, $V(t)$ is the moving control volume and $S(t)$ its boundary, which is assumed to move with an arbitrary local velocity $\boldsymbol{U}_g$. Let $\boldsymbol{N}$ denote the unit outward normal vector to the moving surface and ρ, $\boldsymbol{U}$, P, E the density, velocity, pressure, and specific total energy of the fluid. The set of previous equations is referred to as the ALE integral form of the Euler equations and can be found in many papers [22,1]. Eq. (1a) expresses the conservation of volume and is equivalent to the local kinematic equation

$$\frac{\mathrm{d}}{\mathrm{d}t}\boldsymbol{X}_g = \boldsymbol{U}_g, \quad \boldsymbol{X}_g(0) = \boldsymbol{x}_g, \tag{2}$$

where $\boldsymbol{X}_g$ is a generic point located on the control volume surface. We note that (1a) is also called the geometric conservation law (GCL). The remaining equations, (1b)–(1d) express the conservation of mass, momentum and total energy. We point out that for $\boldsymbol{U}_g = \boldsymbol{U}$, we recover the Lagrangian description of the fluid flow for which the control volume moves with the fluid velocity. On the other hand, for $\boldsymbol{U}_g = \boldsymbol{0}$, we get the classical Eulerian description. The thermodynamical closure of the set of previous equations is obtained by the addition of an equation of state which is taken to be of the form $P = P(\rho,\varepsilon)$, where the specific internal energy, ε, is related to the specific total energy by $\varepsilon = E - \frac{1}{2}\|\boldsymbol{U}\|^2$.

2.2. Flowchart of the multi-material ALE algorithm

In Fig. 1 we display the flowchart of our multi-material ALE method. The multi-material modeling can be done using either the Volume Of Fluid capability or concentration equations. The initialization stage consists in defining the distribution

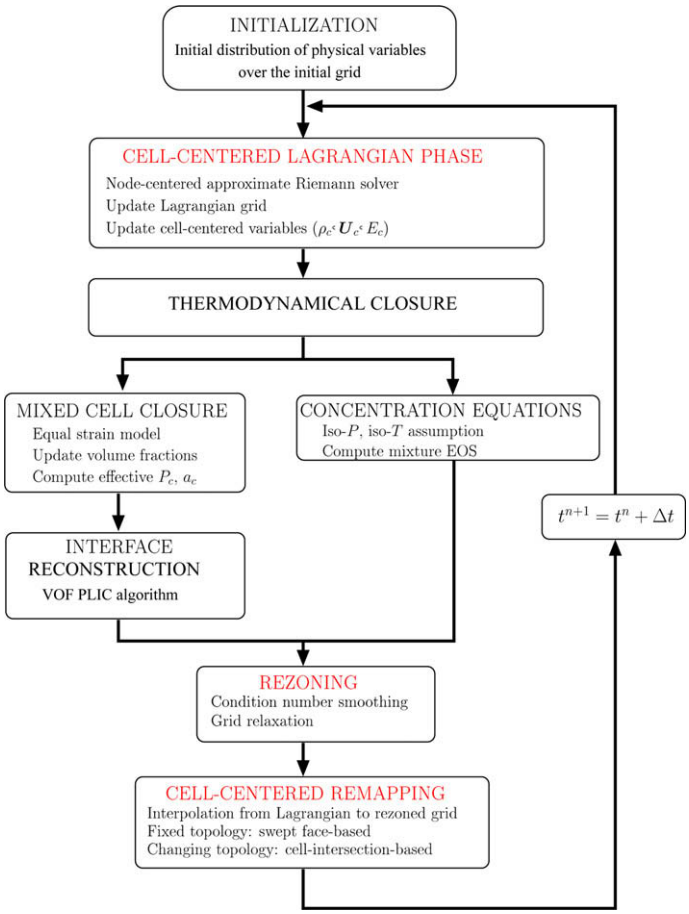

Fig. 1. Flowchart of the multi-material ALE algorithm.

of all the physical variables over the initial grid. We note that the initialization of the volume fractions or the concentrations, when the interface between two materials is not superimposed with cell edges, is performed by computing the intersection of the interface with the initial grid. During the Lagrangian phase, the gas dynamics equations are solved using a cell-centered moving mesh method, refer to Section 3. Namely, the cell-centered density, ρ_c, velocity, U_c, and total energy, E_c, are updated from time t^n to time $t^{n+1} = t^n + \Delta t$. Using a node-centered approximate Riemann solver, nodal velocity, $\boldsymbol{U}_p$, is computed. This allows to update the Lagrangian grid from t^n to t^{n+1}. For cells containing more than one material, we need to define a thermodynamical closure to update the pressure. This task is described in Section 4. It consists in defining a mixture equation of state for the concentration equations modeling or a mixed cell closure for the VOF modeling. In the latter approach, we also proceed to the interface reconstruction using a Piecewise Linear Interface Construction (PLIC), refer to Section 5. The improvement of the quality of the Lagrangian grid is performed by means of the rezoning phase, refer to Section 6. This step is split into a grid smoothing procedure and a grid relaxation algorithm which keeps the rezoned grid as close as possible to the Lagrangian grid. Finally, in the remapping stage, refer to Section 7, we conservatively interpolate all the physical variables from the Lagrangian grid at time t^{n+1} onto the new rezoned grid deduced from the relaxation procedure. Two approaches are available: the swept face-based remapping and the cell-intersection based remapping. The former is used when the connectivity between the two grids is constant while the latter is employed in case of changing topology.

3. Lagrangian phase

The Lagrangian phase consists in computing the rates of change of volume, mass, momentum and energy, assuming that the computational volumes are following the material motion. By setting $\boldsymbol{U}_g = \boldsymbol{U}$ in the set of Eqs. (1) one gets

$$\frac{\mathrm{d}}{\mathrm{d}t}\int_{V(t)} \mathrm{d}V - \int_{S(t)} \boldsymbol{U}\cdot\boldsymbol{N}\,\mathrm{d}S = 0, \tag{3a}$$

$$\frac{\mathrm{d}}{\mathrm{d}t}\int_{V(t)} \rho\,\mathrm{d}V = 0, \tag{3b}$$

$$\frac{\mathrm{d}}{\mathrm{d}t}\int_{V(t)}\rho \boldsymbol{U}\,\mathrm{d}V+\int_{S(t)}P\boldsymbol{N}\,\mathrm{d}S=\boldsymbol{0}, \tag{3c}$$

$$\frac{\mathrm{d}}{\mathrm{d}t}\int_{V(t)}\rho E\,\mathrm{d}V+\int_{S(t)}P\boldsymbol{U}\cdot\boldsymbol{N}\,\mathrm{d}S=0, \tag{3d}$$

where $V(t)$ is the Lagrangian (material) control volume, $S(t)$ is its surface, and the time rates of change refer to quantities associated with this volume. In this case, the local kinematic equation is written as

$$\frac{\mathrm{d}}{\mathrm{d}t}\boldsymbol{X}=\boldsymbol{U},\quad \boldsymbol{X}(0)=\boldsymbol{x}. \tag{4}$$

In what follows, we recall briefly the cell-centered Lagrangian scheme which has been derived in [38]. Let us point out that this cell-centered scheme is compatible with the GCL in the sense that nodal velocity and numerical fluxes are computed consistently by means of a node-centered solver. Moreover, this scheme is conservative and satisfies an entropy inequality in its first-order semi-discrete form. Before proceeding further, let us introduce some specific notations. Let $\{c\}$ be a collection of nonoverlapping polygons whose union covers the domain filled by the fluid. Each cell is labeled with a unique index c and is denoted by Ω_c. We denote by $\{p\}$ the set of all the vertices of the cells. Each vertex is labeled with a unique index p. If we consider a given cell c, we introduce the set of all vertices of the cell c and denote it by $\mathcal{P}(c)$. For a given node p, we also define the set of all cells that share this vertex and denote it by $\mathcal{C}(p)$. The sets $\mathcal{P}(c)$ and $\mathcal{C}(p)$ are counterclockwise ordered. For a node $p\in\mathcal{P}(c)$, p^- and p^+ are the previous/next nodes with respect to p in the list of vertices of cell c, see Fig. 2. We denote by L_{pc}^- and L_{pc}^+ the half length of the edges $[p^-,p]$ and $[p,p^+]$. We use the same notation to define the unit normal outward $\boldsymbol{N}_{pc}^-$ and $\boldsymbol{N}_{pc}^+$, refer to Fig. 2. We also introduce the corner normal $L_{pc}\boldsymbol{N}_{pc}$ defined by

$$L_{pc}\boldsymbol{N}_{pc}=L_{pc}^-\boldsymbol{N}_{pc}^-+L_{pc}^+\boldsymbol{N}_{pc}^+,$$

knowing that $\boldsymbol{N}_{pc}^2=1$.

All fluid variables are assumed to be constant in cell c and we denote them by using subscript c. Therefore, we obtain a spatial approximation which is first-order accurate. The set of evolution equations for the discrete unknowns $\left(\frac{1}{\rho_c},\boldsymbol{U}_c,E_c\right)$ is written using the Lagrangian conservation equations in control volume form applied to cell c

$$m_c\frac{\mathrm{d}}{\mathrm{d}t}\left(\frac{1}{\rho_c}\right)-\sum_{p\in\mathcal{P}(c)}L_{pc}\boldsymbol{N}_{pc}\cdot\boldsymbol{U}_p=0, \tag{5a}$$

$$m_c\frac{\mathrm{d}}{\mathrm{d}t}\boldsymbol{U}_c+\sum_{p\in\mathcal{P}(c)}\left(L_{pc}^-\Pi_{pc}^-\boldsymbol{N}_{pc}^-+L_{pc}^+\Pi_{pc}^+\boldsymbol{N}_{pc}^+\right)=\boldsymbol{0}, \tag{5b}$$

$$m_c\frac{\mathrm{d}}{\mathrm{d}t}E_c+\sum_{p\in\mathcal{P}(c)}\left(L_{pc}^-\Pi_{pc}^-\boldsymbol{N}_{pc}^-+L_{pc}^+\Pi_{pc}^+\boldsymbol{N}_{pc}^+\right)\cdot\boldsymbol{U}_p=0. \tag{5c}$$

The mesh motion is governed by the local kinematic equation, which in its discrete form at point p writes

$$\frac{\mathrm{d}}{\mathrm{d}t}\boldsymbol{X}_p=\boldsymbol{U}_p,\quad \boldsymbol{X}_p(0)=\boldsymbol{x}_p, \tag{6}$$

where $\boldsymbol{X}_p=(X_p,Y_p)^t$ denotes the coordinates of point p at time $t>0$ and $\boldsymbol{x}_p$ its initial position.

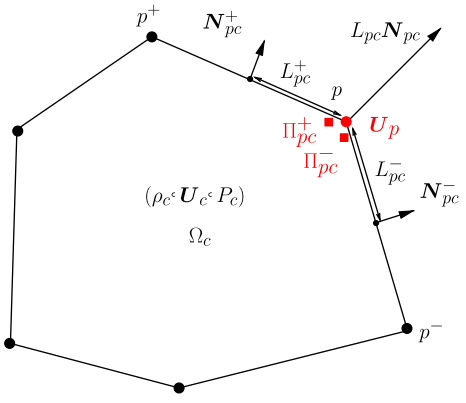

Fig. 2. Fragment of a Lagrangian: notations related to a polygonal cell.

In the above equations, $\boldsymbol{U}_p$ denotes the velocity of the point p and Π^-_{pc}, Π^+_{pc} are nodal pressures located at point p. These pressures can be seen as nodal pressures viewed from cell c and related to the two edges impinging at node p, refer to Fig. 2. These nodal quantities are obtained through the use of a nodal solver which reads

$$\boldsymbol{U}_p = \mathsf{M}_p^{-1} \sum_{c\in\mathcal{C}(p)} [L_{pc}P_c\boldsymbol{N}_{pc} + \mathsf{M}_{pc}\boldsymbol{U}_c], \tag{7a}$$

$$P_c - \Pi^-_{pc} = Z^-_{pc}(\boldsymbol{U}_p - \boldsymbol{U}_c)\cdot\boldsymbol{N}^-_{pc}, \tag{7b}$$

$$P_c - \Pi^+_{pc} = Z^+_{pc}(\boldsymbol{U}_p - \boldsymbol{U}_c)\cdot\boldsymbol{N}^+_{pc}, \tag{7c}$$

where P_c denotes the cell-centered pressure and M_{pc}, M_p are 2×2 matrices which write

$$\mathsf{M}_{pc} = Z^-_{pc}L^-_{pc}(\boldsymbol{N}^-_{pc}\otimes\boldsymbol{N}^-_{pc}) + Z^+_{pc}L^+_{pc}(\boldsymbol{N}^+_{pc}\otimes\boldsymbol{N}^+_{pc}), \quad \mathsf{M}_p = \sum_{c\in\mathcal{C}(p)}\mathsf{M}_{pc}.$$

Here, $Z^\pm_{pc}$ stands for swept mass flux, which according to [14] can be expressed as

$$Z^\pm_{pc} = \rho_c[a_c + \Gamma_c|(\boldsymbol{U}_p - \boldsymbol{U}_c)\cdot\boldsymbol{N}^\pm_{pc}|],$$

where a_c is the isentropic sound speed in cell c and Γ_c is a material dependent parameter, which is defined by setting $\Gamma_c = \frac{\gamma_c+1}{2}$ in the case of a perfect gas.

Let us remark that the M_{pc} matrices are symmetric positive definite, thus providing a M_p matrix which is also symmetric positive definite and hence always invertible. We point out that Eqs. (7b) and (7c) stand for Riemann invariants along the unit outward normal directions. Finally, we get a first-order cell-centered discretization of the Lagrangian hydrodynamics equations based on a node flux discretization. It is shown in [38], that this discretization leads to a conservative and entropy consistent scheme in which the fluxes and the mesh motion are computed in a compatible way so that the GCL is exactly fulfilled at the discrete level.

The accuracy of the present scheme is improved thanks to a high-order extension which uses a two-dimensional version of the generalized Riemann problem (GRP) methodology [7]. This high-order Lagrangian scheme is precisely described in [37].

4. Thermodynamical closures for multi-material flows

In this section we describe two different approaches to deal with thermodynamical closure in the case of a multi-material flow. This closure is required since during the remapping phase of our ALE algorithm the different fluids will flow through the cell edges.

4.1. Multi-material modeling using concentration equations

In this approach, the multi-material fluid flow is viewed as multi-component fluid mixture wherein the kth fluid is characterized by its mass fraction C_k, i.e. the ratio between the mass of fluid k and the total mass of the mixture. We assume that any components are completely miscible from a continuum view point. This assumption applies to gases or materials at high temperatures, i.e. plasmas. During the Lagrangian phase, the concentration of each fluid evolves following the very simple equation $\frac{\mathrm{d}}{\mathrm{d}t}C_k = 0$, that is the concentration of each fluid remains constant during the Lagrangian phase. Consequently, concentration stands for a passive scalar which allows to trace the location of each material inside the flow. We use a pressure–temperature equilibrium assumption to derive the multi-species thermodynamical closure model. Doing that, we obtain an effective equation of state for our multi-component fluid mixture. We suppose that each fluid follows a gamma gas law, namely its pressure, P_k, and specific internal energy, ε_k, write as function of temperature T_k

$$P_k = \frac{R}{\mathcal{M}_k}\rho_k T_k, \quad \varepsilon_k = \frac{R}{(\gamma_k - 1)\mathcal{M}_k}T_k,$$

where R denotes the perfect gas constant, γ_k the polytropic index of fluid k and $\mathcal{M}_k$ its molar mass. The mixture EOS closure problem requires finding the equilibrium mixture pressure, P, and temperature, T, such that the following properties hold:

- Volume conservation: $\frac{1}{\rho} = \sum_{k=1}^K \frac{C_k}{\rho_k}$.
- Energy conservation: $\varepsilon = \sum_{k=1}^K C_k\varepsilon_k$.
- Pressure equilibrium: $P_k = P$, $\forall k = 1,\ldots,K$.
- Temperature equilibrium: $T_k = T$, $\forall k = 1,\ldots,K$.

Here, K denotes the total number of fluids, ρ, ε are the density and the specific internal energy of the mixture and ρ_k, ε_k the density and specific internal energy of fluid k. The solution of the previous set of equations allows to write the following effective mixture gamma gas law

$$P = (\gamma - 1)\rho\varepsilon,$$

where γ is the effective polytropic index of the mixture, which writes

$$\gamma = 1 + \frac{\sum_{k=1}^{K} \frac{C_k}{\mathcal{M}_k}}{\sum_{k=1}^{K} \frac{C_k}{(\gamma_k - 1)\mathcal{M}_k}}. \tag{8}$$

4.2. Multi-material modeling using Volume Of Fluid capability

In this second approach, we assume that the materials are immiscible. The Volume Of Fluid (VOF) methodology introduces a Lagrangian tracking capability for material interfaces into our ALE algorithm. Thus, we have to deal with mixed cells that contain different materials. The mixed cell modeling is based on the knowledge of the volume fractions. Being given the volume of the mixed cell, V, and the volume occupied by the kth fluid, V_k, the corresponding volume fraction writes $\phi_k = \frac{V_k}{V}$. The main issue related to the mixed cell is to define its evolution during the Lagrangian phase. Namely, knowing the total change of volume, momentum and energy how should they be distributed between materials. This is done using a closure model that allows to compute an effective thermodynamical state in the mixed cell as function of the thermodynamical states of the materials and the volume fractions. Here, we briefly recall the closure model based on the assumption of equal strain rates [46]. As noticed by Benson [8], this assumption is clearly incorrect if we apply it to a mixture of air and steel for instance. However, in spite of this crude approximation, this simple model is rather robust and gives quite acceptable results. More sophisticated models based on the physical assumption of pressure relaxation are also available [4,47,24].

Let us denote by m_k the partial mass of material k in the mixed cell. The total mass, m, writes obviously $m = \sum_k m_k$. Using the definition of the volume fraction one gets

$$\frac{m_k}{m} = \frac{\rho_k}{\rho}\phi_k, \tag{9}$$

where ρ and ρ_k denote the global and the partial density of mass in the mixed cell. The time differentiation of (9) gives

$$\rho_k \frac{\mathrm{d}\phi_k}{\mathrm{d}t} = \rho_k \phi_k \left(\frac{1}{\rho}\frac{\mathrm{d}\rho}{\mathrm{d}t} - \frac{1}{\rho_k}\frac{\mathrm{d}\rho_k}{\mathrm{d}t} \right). \tag{10}$$

Since by assumption the volumetric strain rate is equal for all materials, i.e. $\frac{1}{\rho}\frac{\mathrm{d}\rho}{\mathrm{d}t} = \frac{1}{\rho_k}\frac{\mathrm{d}\rho_k}{\mathrm{d}t}$, we conclude that during the Lagrangian phase the volume fraction of each material is constant

$$\phi_k^{n+1} = \phi_k^n. \tag{11}$$

We note that this equal strain assumption is consistent with the fact that the materials in the mixed cell have the same velocity field, $\boldsymbol{U}$, which is nothing but the Lagrangian cell-centered velocity of the mixed cell.

At the end of the Lagrangian phase, being given the volume of the mixed cell, V^{n+1}, and the volume fractions ϕ_k^{n+1}, we update the partial densities as

$$\rho_k^{n+1} = \frac{m_k}{\phi_k^{n+1} V^{n+1}}. \tag{12}$$

Knowing the volume fractions and the partial pressures, P_k, it remains to determine the effective pressure, P, in the mixed cell. To this end, we write the time variation of internal energy for each material using the Gibbs relation

$$\rho_k \frac{d\varepsilon_k}{dt} + P_k \rho_k \frac{d}{dt}\left(\frac{1}{\rho_k}\right) = \rho_k T_k \frac{ds_k}{dt}. \tag{13}$$

Here, T_k and s_k denote the temperature and the specific entropy for material k. We multiply this equation by ϕ_k, sum over all materials, use energy conservation ($m\varepsilon = \sum_k m_k \varepsilon_k$) and apply the equal strain assumption to get

$$\rho \frac{d\varepsilon}{dt} + \sum_k \phi_k P_k \rho \frac{d}{dt}\left(\frac{1}{\rho}\right) = \sum_k \phi_k \rho_k T_k \frac{ds_k}{dt}.$$

The comparison of this relation and the effective Gibbs relation written for the mixture

$$\rho \frac{d\varepsilon}{dt} + P\rho \frac{d}{dt}\left(\frac{1}{\rho}\right) = \rho T \frac{ds}{dt}, \tag{14}$$

allows to define the effective pressure as

$$P = \sum_k \phi_k P_k. \tag{15}$$

We also define the effective sound speed, a, knowing the sound speed of each material, i.e. $a_k^2 = \left(\frac{dP_k}{d\rho_k}\right)_{s_k}$. We differentiate (15), knowing that ϕ_k is constant and using the equal strain assumption to get

$$a = \left(\sum_k \phi_k \frac{\rho_k}{\rho} a_k^2 \right)^{\frac{1}{2}}. \tag{16}$$

This effective sound speed is used in our node-centered Riemann solver to compute the numerical fluxes, refer to Eqs. (7).

Finally, it remains to update the internal energy for each material. Since we are using a Godunov-type method to discretize Lagrangian hydrodynamics, internal energy is calculated as the difference between the total energy of the zone and its kinetic energy. Namely, at the discrete level, the mixed cell internal energy variation is written

$$m(\varepsilon^{n+1} - \varepsilon^n) = m\left[E^{n+1} - E^n - \frac{1}{2}\{(\boldsymbol{U}^{n+1})^2 - (\boldsymbol{U}^n)^2\} \right].$$

Knowing the effective internal energy variation, we compute the global heating over the mixed cell as

$$\delta Q = m(\varepsilon^{n+1} - \varepsilon^n) + P^n(V^{n+1} - V^n), \tag{17}$$

we note that this global heating corresponds to the approximation of the Gibbs relation (14) written for the mixed cell. We compute the partial internal energy variation for each material by making the assumption that the global heating is distributed over each material as

$$m_k(\varepsilon_k^{n+1} - \varepsilon_k^n) + P_k^n(V_k^{n+1} - V_k^n) = \phi_k \delta Q. \tag{18}$$

Let us remark that this formulation conserves energy in the sense that $\sum_k m_k(\varepsilon_k^{n+1} - \varepsilon_k^n) = m(\varepsilon^{n+1} - \varepsilon^n)$, due to the definition of the effective pressure, i.e. $P^n V^n = \sum_k P_k^n V_k^n$ and $P^n V^{n+1} = \sum_k P_k^n V_k^{n+1}$. We also point out that this distribution of heating over the materials amounts to prescribe at the continuum level $\rho_k T_k \frac{ds_k}{dt} = \rho T \frac{ds}{dt}$. In other words, we apply an equal time rate of volumetric heating for both the mixed cell and the materials.

Comment 1. The main reason for also presenting the concentration equations approach as well as the VOF treatment lies in the fact that we want to make comparisons to demonstrate the benefits of the VOF approach.

5. Interface reconstruction

The method used to reconstruct the interface is an extension to the case of general unstructured polygonal grid of the algorithm initially designed by Youngs [51]. The goal of the method is to perform a Piecewise Linear Interface Construction (PLIC) in each mixed cell, being given the volume fraction of each fluid. We make the fundamental assumption that each mixed cell contains two immiscible fluids. For a given cell Ω_c, each fluid is characterized by its volume fraction $\phi_{c,k}$, $k = 1, 2$, which stands for the ratio between the volume occupied by the fluid and the total volume of the cell. Obviously, $\phi_{c,k}$ satisfies $0 \leqslant \phi_{c,k} \leqslant 1$ and $\phi_{c,1} + \phi_{c,2} = 1$. We define the reference volume fraction by setting $\phi_c^{\text{ref}} = \phi_{c,1}$. Knowing ϕ_c^{ref} we construct the interface as one segment of straight line cutting the mixed cell into two pure regions. This line is defined in each cell by the equation

$$\boldsymbol{N}_c \cdot \boldsymbol{X} + d_c = 0, \tag{19}$$

where $\boldsymbol{X}$ stands for the position vector of a generic point located on the line, $\boldsymbol{N}_c$ is the unit normal vector to the line, and d_c is the signed distance from the line to the origin of the Cartesian orthonormal frame $(0, X, Y)$.

The first step of the interface reconstruction consists in computing an approximate unit normal $\boldsymbol{N}_c$ in each cell c. This normal is evaluated using the following formula

$$\boldsymbol{N}_c = -\frac{\nabla \phi_c}{\|\nabla \phi_c\|}.$$

Here $\nabla \phi_c$ denotes the gradient of the volume fraction. Although ϕ is not a smooth function, we compute its gradient using a least squares approach. In each cell c, we assume a piecewise linear representation of the volume fraction by writing

$$\tilde{\phi}_c(\boldsymbol{X}) = \phi_c^{\text{ref}} + \nabla \phi_c \cdot (\boldsymbol{X} - \boldsymbol{X}_c),$$

where $\nabla \phi_c$ is the constant gradient of the volume fraction and $\boldsymbol{X}_c$ is the centroid of the cell. Thus, $\nabla \phi_c$ is obtained by solving the minimization problem

$$\nabla \phi_c = \underset{\boldsymbol{A} \in \mathbb{R}^2}{\operatorname{argmin}} \sum_{d \in \mathcal{C}(c)} [\phi_d^{\text{ref}} - \phi_c^{\text{ref}} - \boldsymbol{A} \cdot (\boldsymbol{X}_d - \boldsymbol{X}_c)]^2.$$

Here, $\mathcal{C}(c)$ denotes the set of the neighbouring cells of cell c. It is well known that this method leads only to a first-order reconstruction of the normal [16,2].

The second step of the reconstruction consists in computing d_c by locating the interface along the normal direction so that the volume cut by the interface coincides with the sub-cell volume computed using the reference volume fraction ϕ_c^{ref}. Knowing the unit normal $\boldsymbol{N}_c$, the location of the moving interface is uniquely defined by the value of the parameter d. Hence,

d being given, the corresponding sub-cell volume fraction can be expressed as a continuous monotonic function of d,$\phi_c(d)$. Thus, d_c is obtained by solving the equation

$$\phi_c(d) = \phi_c^{\text{ref}},$$

which has always a unique solution, refer to [16,2] for the details about the numerical implementation.

6. Rezoning phase

The rezoning phase consists in moving the node of the Lagrangian grid to improve the geometric quality of the grid while keeping the rezoned grid as close as possible to the Lagrangian grid. This constraint must be taken into account to maintain the accuracy of the computation brought by the Lagrangian phase. In fact, by requiring the rezoned grid to remain as close as possible to the Lagrangian grid, we minimize the error of the remap phase, and we justify employing a local remapper in which mass, momentum and energy are simply exchanged between neighboring cells. In what follows, we first describe our grid smoothing algorithm which is the condition smoothing algorithm introduced by Knupp [26] for mesh quality optimization. Then, we present a grid relaxation algorithm which intends to keep the rezoned grid in the vicinity of the Lagrangian grid. This grid relaxation procedure represents the most original contribution of this paper.

6.1. Condition number smoothing

We describe the condition number smoothing (CNS) algorithm, which is an unstructured extension of the well-known Winslow algorithm as demonstrated in [28]. We make the assumption that the input grid (the grid produced by the Lagrangian phase) is unfolded. If the Lagrangian phase produces nonvalid cells then we use an untangling procedure [48]. We first recall the condition number smoothing algorithm for an internal node, then we present an original extension to the case of nodes located on a boundary.

6.1.1. Internal node

Let c be a given cell of the Lagrangian grid, $p \in \mathcal{P}(c)$ a particular node of this cell and p^-, p^+ the previous and next nodes with respect to p in the counterclockwise list of the vertices of cell c, refer to Fig. 3. Let $\mathrm{J}_{cp} = [\boldsymbol{pp}^+|\boldsymbol{pp}^-]$ be the 2×2 Jacobian matrix associated with each corner at a vertex p of cell c. It is shown in [26] that the condition number of matrix J_{cp} in $\mathbb{R}^2$ writes

$$\kappa(\mathrm{J}_{cp}) = \frac{\|\boldsymbol{pp}^+\|^2 + \|\boldsymbol{pp}^-\|^2}{A_{cp}}, \tag{20}$$

where A_{cp} is the area of the triangle whose vertices are p^-, p, p^+. We note that κ is minimal for an isosceles rectangular triangle. With this condition number, we define the local objective function associated to node p

$$F_p(\boldsymbol{X}_p) = \sum_{c \in \mathcal{C}(p)} \sum_{q \in \mathcal{V}_c(p)} \kappa(\mathrm{J}_{cq}). \tag{21}$$

Here $\boldsymbol{X}_p$ denotes the vector position of point p, $\mathcal{C}(p)$ is the set of cells that share node p and $\mathcal{V}_c(p)$ is the set of vertices of cell c that are connected to vertex p (including p itself). By summing this functional over all grid nodes, we can also define a global objective function.

One very important feature that can be seen explicitly in the definition of $\kappa(\mathrm{J}_{cp})$ is that the functional has a barrier, i.e., the value of the functional approaches infinity when the new grid contains a nonvalid grid for which $A_{cp} = 0$. This explains how the condition number smoothing produces unfolded grids.

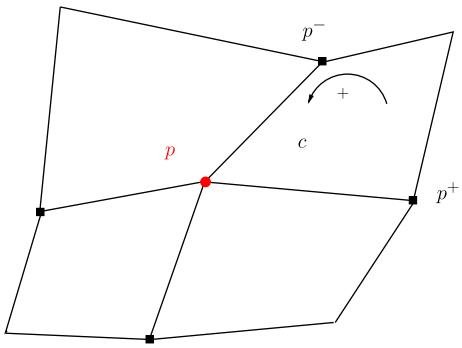

Fig. 3. Fragment of a grid: notations for condition number smoothing.

The rezoned position of node p, $\boldsymbol{X}_p^{\text{rez}}$, is determined by minimizing the local functional (21) using the first step of a Newton algorithm

$$\boldsymbol{X}_p^{\text{rez}} = \boldsymbol{X}_p^{n+1,\text{lag}} - \mathsf{H}_p^{-1}(\boldsymbol{X}_p^{n+1,\text{lag}})\nabla F_p(\boldsymbol{X}_p^{n+1,\text{lag}}), \tag{22}$$

where $\boldsymbol{X}_p^{n+1,\text{lag}}$ denotes the vector position of point p at the end of the Lagrangian phase and H_p is the 2×2 Hessian matrix related to F_p. We note that the computation of the Hessian and the gradient of the functional are performed using the coordinates of the points at the end of the Lagrangian phase. We separately minimize each of the local objective functions and iterate over all the nodes. This approach is termed as Jacobi sweep minimization. Its main advantage lies in the fact that it does not depend on the vertex order and thus leads to a symmetry preserving algorithm.

6.1.2. Boundary node

Let p denotes a boundary node and p^-, p^+ its previous and next neighbors in the list of boundary nodes, refer to Fig. 4. To define the rezoned position of node p in a consistent manner with the condition number smoothing algorithm, we first determine a piecewise parametric representation of the boundary. To this end we introduce the second-order interpolation Bézier curve

$$\boldsymbol{X}_p(t) = (1-t)^2\boldsymbol{X}_{p^-} + 2(1-t)t\boldsymbol{X}_i + t^2\boldsymbol{X}_{p^+}, \quad t\in[0,1] \tag{23}$$

where $\boldsymbol{X}_i$ denotes the vector position of point i, which is a control point of the Bézier curve. This control point is defined so that the Bézier curve passes through point p. Hence, for a given $t_0\in\,]0,1[$, $\boldsymbol{X}_i$ is computed by setting $\boldsymbol{X}_p(t_0) = X_p$, this leads to

$$\boldsymbol{X}_i = \frac{\boldsymbol{X}_p - (1-t_0)^2\boldsymbol{X}_{p^-} - t_0^2\boldsymbol{X}_{p^+}}{2(1-t_0)t_0}. \tag{24}$$

The parameter t_0 is usually defined by setting $t_0 = \frac{1}{2}$. Using the parametric representation of the boundary curve, we define the nodal objective functional related to node p by setting

$$f_p(t) = F_p(\boldsymbol{X}_p(t)), \tag{25}$$

where F_p is the functional defined by (21). Using the chain rule we get

$$\frac{\mathrm{d}f_p}{\mathrm{d}t} = \nabla F_p\cdot\frac{\mathrm{d}}{\mathrm{d}t}\boldsymbol{X}_p(t), \quad \frac{\mathrm{d}^2 f_p}{\mathrm{d}t^2} = \mathsf{H}_p\frac{\mathrm{d}}{\mathrm{d}t}\boldsymbol{X}_p(t)\cdot\frac{\mathrm{d}}{\mathrm{d}t}\boldsymbol{X}_p(t) + \nabla F_p\cdot\frac{\mathrm{d}^2}{\mathrm{d}t^2}\boldsymbol{X}_p(t).$$

Finally, to find the rezoned position of point p, it remains to minimize the real function $f_p(t)$. To this end, we perform one step of a Newton procedure to compute

$$t^{\text{rez}} = t_0 - \frac{\frac{\mathrm{d}f_p}{\mathrm{d}t}(t_0)}{\frac{\mathrm{d}^2 f_p}{\mathrm{d}t^2}(t_0)}. \tag{26}$$

After checking that $t^{\text{rez}}\in[0,1]$ the vector position of the rezoned point is defined as $\boldsymbol{X}_p^{\text{rez}} = \boldsymbol{X}_p(t^{\text{rez}})$. We note that this boundary node treatment performs particularly well in the case of free boundary condition.

6.2. Relaxation algorithm

The updated location of the node is defined by mean of a convex combination between its rezoned location obtained from the previous CNS method and its location at the end of the Lagrangian phase

$$\boldsymbol{X}^{n+1} = \boldsymbol{X}^{n+1,\text{lag}} + \omega_p(\boldsymbol{X}^{\text{rez}} - \boldsymbol{X}^{n+1,\text{lag}}),$$

where $\omega_p\in[0,1]$ is a node-based coefficient computed as a function of the invariants of the right Cauchy–Green strain tensor, which is associated to the deformation of the Lagrangian grid over a time step. Let us briefly recall the definition of these tensors which are basic tools in the framework of continuum mechanics, refer to [9]. For sake of conciseness, let $\boldsymbol{X}^0$ and $\boldsymbol{X}^1$

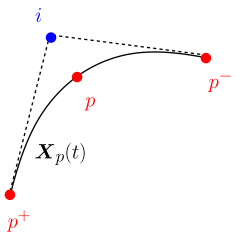

Fig. 4. Boundary node treatment: notations for the Bézier curve. p^-, p and p^+ are vertices located on the boundary. The second-order interpolation Bézier curve, $\boldsymbol{X}_p(t)$ is plotted in black.

denote the position vector of a generic point associated to the Lagrangian grid at time t^n and at time $t^{n+1} = t^n + \Delta t$. We assume that these two grids are valid, hence we can define a one to one map between these two configurations of the flow by setting $\boldsymbol{X}^1 = \boldsymbol{\Psi}(\boldsymbol{X}^0, \Delta t)$. This map is characterized by its Jacobian matrix

$$\mathsf{F} = \frac{\partial \boldsymbol{\Psi}}{\partial \boldsymbol{X}^0},$$

which is also named the deformation gradient tensor and can be explicitly written in $\mathbb{R}^2$ as

$$\mathsf{F} = \begin{pmatrix} \frac{\partial X^1}{\partial X^0} & \frac{\partial X^1}{\partial Y^0} \\ \frac{\partial Y^1}{\partial X^0} & \frac{\partial Y^1}{\partial Y^0} \end{pmatrix},$$

where $\boldsymbol{X}^0 = (X^0, Y^0)^t$ and $\boldsymbol{X}^1 = (X^1, Y^1)^t$. We also introduce the determinant of the Jacobian matrix, $J = \det \mathsf{F}$, which is strictly positive since the grids are valid. The right Cauchy–Green strain tensor, C, is obtained by right-multiplying F by its transpose, $\mathsf{C} = \mathsf{F}^t\mathsf{F}$. In our case, C is a 2×2 symmetric positive definite tensor. We notice that this tensor reduces to the unitary tensor in case of uniform translation or rotation. It admits two positive eigenvalues, which are denoted λ_1 and λ_2 with the convention $\lambda_1 \leqslant \lambda_2$. These eigenvalues can be viewed as the rates of dilation in the eigenvectors directions of the transformation. The definition of the ω_p factor as a function of the invariants of the right Cauchy–Green tensor leads to mesh relaxation procedure which satisfies the principle of Galilean invariance, that is either for a uniform translation or a pure rotation the relaxed mesh coincides with the Lagrangian one. It remains to construct a node-centered approximation of the Cauchy–Green tensor. To this end we use the Nanson formula [9] which expresses the change of length between the two Lagrangian configurations labeled (0) and (1). This formula writes

$$J(\mathsf{F}^{-1})^t \boldsymbol{N}^0 \, \mathrm{d}L^0 = \boldsymbol{N}^1 \, \mathrm{d}L^1, \tag{27}$$

where $\mathrm{d}L^0$ and $\mathrm{d}L^1$ are the length elements in the configurations (0) and (1) and $\boldsymbol{N}^0$, $\boldsymbol{N}^1$ their corresponding unit outward normals. Introducing $\mathsf{K} = J(\mathsf{F}^{-1})^t$, the Nanson formula reads

$$\mathsf{K}\boldsymbol{N}^0 \, \mathrm{d}L^0 = \boldsymbol{N}^1 \, \mathrm{d}L^1. \tag{28}$$

We will use these last formula to compute K and then deduce F. To this end, let us consider a cell Ω_c and one of its vertices p. As usual, we denote p^- and p^+ the previous and the next vertex to p in the counterclockwise list of vertices of cell c. We display in Fig. 5 the fragments of cell c related to point p for the two Lagrangian configurations (0) and (1). The vectors $L^{0,-}_{pc}\boldsymbol{N}^{0,-}_{pc}$, $L^{0,+}_{pc}\boldsymbol{N}^{0,+}_{pc}$ and $L^{1,-}_{pc}\boldsymbol{N}^{1,-}_{pc}$, $L^{1,+}_{pc}\boldsymbol{N}^{1,+}_{pc}$ are the half outward normals related to point p and cell c for the two configurations. Let us denote K_{pc} the local approximation of the tensor K for cell c at point p. It is defined by applying the Nanson formula (28) as follows

$$\mathsf{K}_{pc} L^{0,-}_{pc}\boldsymbol{N}^{0,-}_{pc} = L^{1,-}_{pc}\boldsymbol{N}^{1,-}_{pc}, \tag{29a}$$

$$\mathsf{K}_{pc} L^{0,+}_{pc}\boldsymbol{N}^{0,+}_{pc} = L^{1,+}_{pc}\boldsymbol{N}^{1,+}_{pc}. \tag{29b}$$

Assuming that the two normals $L^{0,-}_{pc}\boldsymbol{N}^{0,-}_{pc}$ and $L^{0,+}_{pc}\boldsymbol{N}^{0,+}_{pc}$ are not colinear, the above system admits always a unique solution. We point out that the above procedure allows to define the tensor K_{pc} for each corner pc that surrounds point p. Finally, to construct the approximation of the tensor K centered at point p, K_p, we solve (29) in the least squares sense by minimizing the functional

$$\mathcal{L}(\mathsf{K}_p) = \frac{1}{2} \sum_{c \in \mathcal{C}(p)} [(\mathsf{K}_p L^{0,-}_{pc}\boldsymbol{N}^{0,-}_{pc} - L^{1,-}_{pc}\boldsymbol{N}^{1,-}_{pc})^2 + (\mathsf{K}_p L^{0,+}_{pc}\boldsymbol{N}^{0,+}_{pc} - L^{1,+}_{pc}\boldsymbol{N}^{1,+}_{pc})^2],$$

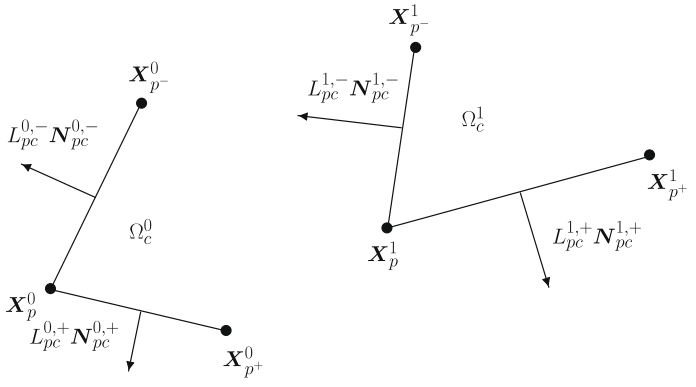

Fig. 5. Fragments of the Lagrangian grids: configuration (0) (left) and configuration (1) (right).

where $\mathcal{C}(p)$ denotes the set of cells that surround point p. The solution of the above minimization problem leads to the approximation of the deformation gradient tensor centered at point p, F_p. Recalling that $\mathsf{K} = J(\mathsf{F}^{-1})^t$, the components of K_p are expressed in terms of the components of F_p as follows

$$\mathsf{K}_p = \begin{pmatrix} F_p^{yy} & -F_p^{yx} \\ -F_p^{xy} & F_p^{xx} \end{pmatrix}.$$

Once the approximation of the deformation gradient tensor centered at point p is determined, the Cauchy–Green tensor is obtained by computing $\mathsf{C}_p = \mathsf{F}_p^t \mathsf{F}_p$. Knowing this symmetric positive definite tensor at each node, we compute its real positive eigenvalues $\lambda_{1,p}$, $\lambda_{2,p}$ and define ω_p as

$$\omega_p = 1 - \frac{\alpha_p - \alpha_{\min}}{1 - \alpha_{\min}}, \tag{30}$$

where $\alpha_p = \frac{\lambda_{1,p}}{\lambda_{2,p}}$ and $\alpha_{\min} = \min_p \alpha_p$. We point out that for uniform translation or rotation $\lambda_{1,c} = \lambda_{2,c} = 1$ and $\omega_p = 0$, therefore the motion of the nodes is purely Lagrangian and we fulfill the material frame indifference requirement. For other cases, ω_p smoothly varies between 0 and 1.

Comment 2. The first role of the ω parameter is to construct a convex combination between the Lagrangian grid and the rezoned grid, that is why we want it to be in $[0,1]$. Moreover, we want it to vanish smoothly for rigid rotation and translation and recover the pure Lagrangian motion in these cases. In a nutshell, we want it to be Galilean invariant. To construct a parameter that fulfills the previous requirements we utilize mechanical object that characterizes properly the mechanical features of the flow. A good candidate for this task is the right Cauchy–Green tensor evaluated between two consecutive Lagrangian time steps. It can be regarded as quantifying the ratio of squared lengths of infinitesimal fibers between the initial and the final configurations [10]. To be more precise, let $\mathrm{d}X_0 = L_0 N_0$ denotes a material fiber of length L_0 in the initial configuration, where N_0 is a unit vector. This elementary fiber is stretched and rotated to $\mathrm{d}X_1 = L_1 N_1$, in the final configuration, where N_1 is a unit vector. Introducing F as the deformation gradient between the initial and the final configuration, one has $\mathrm{d}X_1 = \mathsf{F}\,\mathrm{d}X_0$. Therefore, one can deduce that the length of the fiber in the final configuration is given by

$$L_1^2 = \mathrm{d}\boldsymbol{X}_1 \cdot \mathrm{d}\boldsymbol{X}_1 = L_0 \mathsf{F}\boldsymbol{N}_0 \cdot L_0 \mathsf{F}\boldsymbol{N}_0 = L_0^2 \mathsf{F}^t \mathsf{F}\boldsymbol{N}_0 \cdot \boldsymbol{N}_0.$$

Hence, the ratio of the squared lengths writes as

$$\left(\frac{L_1}{L_0}\right)^2 = \mathsf{C}\boldsymbol{N}_0 \cdot \boldsymbol{N}_0,$$

where $\mathsf{C} = \mathsf{F}^t\mathsf{F}$ is the Cauchy–Green tensor, which is symmetric definite positive and fulfills the requirements of Galilean invariance. Here, the subscripts 0 and 1 refer to the initial and final configurations corresponding to the beginning and the end of the Lagrangian time step. As it can be observed in Fig. 25 for the interaction of a shock wave with an Helium bubble, refer to Section 8.4, this parameter is a good indicator to track accurately the compression waves that interact inside complex two-dimensional flow.

7. Remapping phase

The remapping phase corresponds to a conservative interpolation of the physical variables from the Lagrangian grid at time t^{n+1} onto the rezoned grid. A cell-centered remapping scheme will now be presented to complement the cell-centered Lagrangian scheme. Let $\{c\}$ and $\{\tilde{c}\}$ be respectively collections of nonoverlapping polygons of the Lagrangian and the rezoned grids. In what follows, we denote all quantities related to the rezoned grid using the tilde accent. Let ψ be a physical variable of the flow defined on $\{c\}$ by its piecewise constant representation ψ_c. Being given ψ_c, we want to compute

$$\psi_{\tilde{c}} = \frac{1}{V(\tilde{c})} \int_{\tilde{c}} \psi \,\mathrm{d}\boldsymbol{X}. \tag{31}$$

That is, knowing the mean value of ψ over each cell of the Lagrangian grid, we want to compute its mean value over each cell of the new rezoned grid. To obtain a sufficiently accurate remapping, we first compute a piecewise monotonic linear reconstruction of the variable ψ over the Lagrangian grid. Namely, knowing the mean value ψ_c, we re-construct the piecewise linear function, $\psi_c(\boldsymbol{X})$, over the Lagrangian cell c as follows

$$\psi_c(\boldsymbol{X}) = \psi_c + (\nabla\psi)_c(\boldsymbol{X} - \boldsymbol{X}_c).$$

Here, $(\nabla\psi)_c$ denotes the constant gradient of ψ within cell c, which is computed using a least squares approach. The monotonicity of this reconstruction is enforced by using the classical Barth–Jespersen slope limitation procedure [6]. We also note that this reconstruction preserves the mean value ψ_c provided that $\boldsymbol{X}_c$ is the centroid of cell c, i.e.

$$\boldsymbol{X}_c = \frac{1}{V(c)} \int_c \boldsymbol{X} \,\mathrm{d}\boldsymbol{X}.$$

In this section we are dealing with remapping methods based on a partition of the volume of the rezoned cell in terms of its overlap with the Lagrangian cells. Following the methodology derived in [41] we have developed two approaches for the remapping phase that are briefly recall in the next two paragraphs.

Comment 3. Here, ψ denotes a physical variable which is defined per unit volume, such as ρ, ρU and ρE. Let θ denotes the corresponding physical variable defined per unit mass, i.e. $\psi = \rho\theta$. Hence, the remapped value of θ over the new cell $\tilde{c}$ reads

$$\theta_{\tilde{c}} = \frac{\psi_{\tilde{c}}}{\rho_{\tilde{c}}},$$

where $\psi_{\tilde{c}}$ and $\rho_{\tilde{c}}$ have been computed using (31).

7.1. Swept face-based method

Here, we briefly present an unstructured extension of the swept integration method presented in [41]. Assuming a fixed topology between the old (Lagrangian) and the new (rezoned) grids, a generic cell of the new grid can be decomposed as

$$\tilde{c} = c \cup \left(\bigcup_{d \in \mathcal{C}(c)\setminus c} (\tilde{c} \cap d) \right) \setminus \left(\bigcup_{\tilde{d} \in \mathcal{C}(\tilde{c})\setminus \tilde{c}} (c \cap \tilde{d}) \right). \tag{32}$$

This decomposition, which is displayed in Fig. 6(left), allows to write the mean value of ψ over the new cell as

$$\psi_{\tilde{c}} = \frac{1}{V(\tilde{c})} \left(\int_c \psi \, \mathrm{d}\boldsymbol{X} + \sum_{d \in \mathcal{C}(c)\setminus c} \int_{\tilde{c}\cap d} \psi \, \mathrm{d}\boldsymbol{X} - \sum_{\tilde{d} \in \mathcal{C}(\tilde{c})\setminus \tilde{c}} \int_{c \cap \tilde{d}} \psi \, \mathrm{d}\boldsymbol{X} \right).$$

Here, the volume of the new cell, $V(\tilde{c})$, is expressed as the volume of the old cell, plus the summation of the signed volumes of the quadrangular regions swept during the displacement of the edges, from their old positions to their new ones. More precisely, each displacement of two consecutive vertices p and p^+ leads to construct the quadrangular swept region $S_{p,p^+} = \{p, \tilde{p}, \tilde{p}^+, p^+\}$ whose volume is denoted $V(S_{p,p^+})$, refer to Fig. 6(right). Using this notation, one obtains

$$V(\tilde{c}) = V(c) + \sum_{\{p,p^+\} \in c} V(S_{p,p^+}).$$

Following this approach, the mean value of ψ over the new cell writes

$$\psi_{\tilde{c}} = \frac{1}{V(\tilde{c})} \left(\int_c \psi \, \mathrm{dX} + \sum_{\{p,p^+\} \in c} \int_{S_{p,p^+}} \psi \, \mathrm{d}\boldsymbol{X} \right).$$

The integral corresponding to the second term in the right-hand side, is the quadrangular swept region contribution to the flux. This integral is approximated in an upwind manner by setting

$$\int_{S_{p,p^+}} \psi \, \mathrm{d}\boldsymbol{X} = \begin{cases} \int_{S_{p,p^+}} \psi_{c^+}(\boldsymbol{X}) \mathrm{d}\boldsymbol{X} & \text{if } V(S_{p,p^+}) \geqslant 0, \\ \int_{S_{p,p^+}} \psi_{c}(\boldsymbol{X}) \mathrm{d}\boldsymbol{X} & \text{if } V(S_{p,p^+}) < 0, \end{cases} \tag{33}$$

where $\psi_{c^+}(\boldsymbol{X})$ and $\psi_c(\boldsymbol{X})$ are piecewise linear reconstruction of the function ψ over the Lagrangian cells c^+ and c.

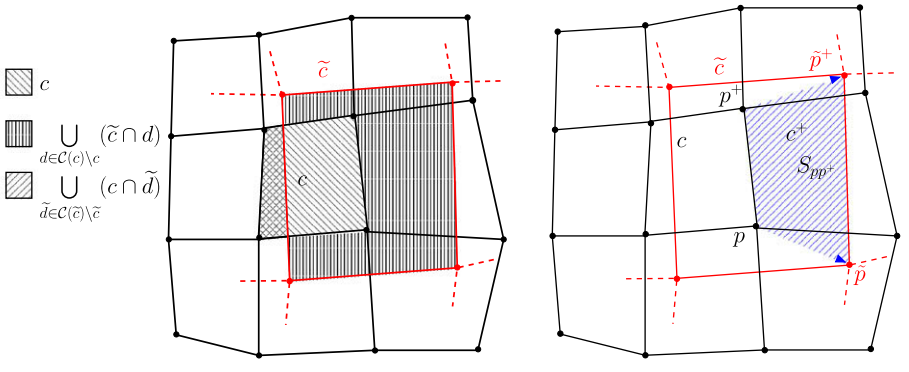

Fig. 6. Decomposition of a rezoned cell (left). Swept region resulting from nodes displacement (right).

7.2. Cell-intersection-based method

This approach is used when we are dealing with an old and a new grids whose connectivities differ. This situation occurs in the vicinity of mixed cells in the case of a multi-material computation using VOF capability for interface tracking. For each rezoned cell, we need to compute exactly its overlap with the surrounding Lagrangian cells. To this end, we employ an exact intersection algorithm which is based on a triangulation of the old and the new grids. The main reason for working with triangles lies in the fact that the intersection between two triangles is always a convex polygon. Let us describe the different steps of this algorithm.

1. **Triangulation**: We perform the triangulation of the Lagrangian and the rezoned grid which are initially paved with non-overlapping polygonal cells. The triangulation of a convex polygon is a trivial operation by simply adding edges from one vertex to all other vertices as it displayed in Fig. 7(left). In the case of a non-convex polygonal cell, one way to triangulate it is by using the assertion that any simple polygon without holes has at least two so called 'ears'. An ear is a triangle with two sides on the edge of the polygon and the other one completely inside it. The algorithm then consists of finding such an ear, removing it from the polygon (which results in a new polygon that still meets the conditions) and repeating until there is only one triangle left. This algorithm is easy to implement and is known as ear clipping algorithm [17]. The triangulation of a non-convex polygon using this algorithm is displayed in Fig. 7(right). Being given a generic Lagrangian cell c and generic rezoned cell $\tilde{c}$, let us denote $\mathcal{T}(c)$ and $\mathcal{T}(\tilde{c})$ their corresponding sets of triangles.
2. **Intersection**: Assuming that the rezoned cell $\tilde{c}$ is located in the neighborhood of the Lagrangian cell c, we compute the intersection of each triangle of $\mathcal{T}(\tilde{c})$ with the triangles of $\mathcal{T}(d)$ for $d \in \mathcal{C}(c)$ where $\mathcal{C}(c)$ is the set of the neighboring cells of cell c. For a given couple of triangles $(T, \widetilde{T})$ in $\mathcal{T}(d) \times \mathcal{T}(\tilde{c})$ with $d \in \mathcal{C}(c)$ the intersection algorithm proceeds as follows. First, using the barycentric coordinates, we determine successively the localization of the vertices of $\mathcal{T}(\tilde{c})$ in $\mathcal{T}(d)$ and the localization of the vertices of $\mathcal{T}(d)$ in $\mathcal{T}(\tilde{c})$. Second, we compute the edges intersection between $\mathcal{T}(\tilde{c})$ and $\mathcal{T}(d)$. To summarize, this just means find the nodes of the old mesh triangles which lie inside new mesh triangles and then find edge intersection points.
3. **Sub-polygon reconstruction**: The triangle–triangle intersection phase leads to a list of points that are the vertices of a convex sub-polygon which is displayed in Fig. 8. We re-order in a counterclockwise manner the list of the vertices of this sub-polygon.
4. **Integration phase**: Let $\mathcal{P}(T \cap \widetilde{T})$ be the set of the intersection sub-polygons between T and $\widetilde{T}$. Finally, the mean value of ψ over the rezoned cell $\tilde{c}$ is computed as

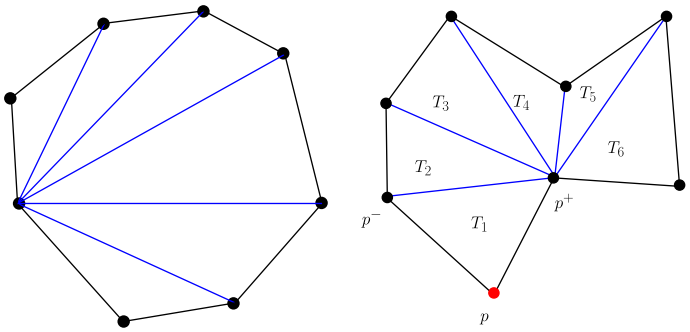

Fig. 7. Triangulation of a convex polygon (left). Triangulation of non-convex polygonal (right) using ear clipping. The algorithm starts at point p which is an ear.

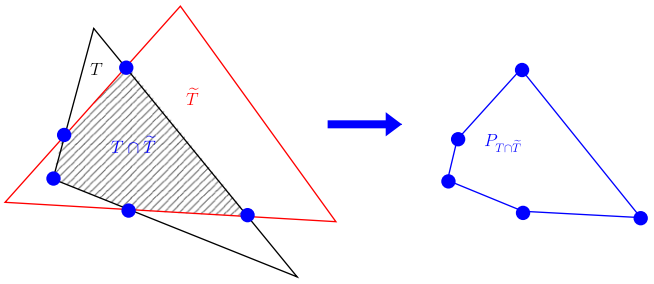

Fig. 8. Sub-polygon that results from triangle–triangle intersection.

$$\psi_{\tilde{c}} = \frac{1}{V(\tilde{c})} \sum_{Q \in \mathcal{P}(T \cap T)} \int_Q \psi_c \, d\boldsymbol{X},$$

where the integrals over the sub-polygons are evaluated using the piecewise linear reconstruction of ψ over the Lagrangian cell. In this computation, the integrals of linear function over a sub-polygon are exactly computed by means of the Green formula [42].

7.3. Mixed cell remapping

Here, we give some details about the remapping of the physical variables in mixed cell when we are using the VOF algorithm. The volume fractions are reconstructed on the rezoned cell as

$$\phi_{\tilde{c},k} = \frac{1}{V(\tilde{c})} \sum_{Q \in \mathcal{P}^k(T \cap T)} \int_Q d\boldsymbol{X}, \tag{34}$$

where $\mathcal{P}^k(\tilde{T} \cap T)$ is the set of intersection sub-polygons, associated to the material k. Let ψ_k be the partial quantity associated to the physical variable ψ which is defined per unit volume. This partial quantity is remapped as

$$\psi_{\tilde{c},k} = \frac{1}{V_k(\tilde{c})} \sum_{Q \in \mathcal{P}^k(T \cap T)} \int_Q \psi_k \, d\boldsymbol{X}, \tag{35}$$

where $V_k(\tilde{c})$ is the partial volume defined on the new cell as $V_k(\tilde{c}) = V(\tilde{c})\phi_{\tilde{c},k}$. Let θ be the corresponding physical variable defined per unit mass and θ_k its related partial quantity. Hence, θ_k is remapped as $\theta_{\tilde{c},k} = \frac{\psi_{\tilde{c},k}}{\rho_{\tilde{c},k}}$ where $\rho_{\tilde{c},k}$ denotes the partial remapped density computed using (35). The partial remapped mass corresponding to material k is computed as $m_{\tilde{c},k} = \rho_{\tilde{c},k} V_k(\tilde{c})$. Finally, the global mass and density over the mixed cells are deduced from

$$m_{\tilde{c}} = \sum_k m_{\tilde{c},k} \quad \text{and} \quad \rho_{\tilde{c}} = \sum_k \rho_{\tilde{c},k} \phi_{\tilde{c},k}.$$

The remaining global quantities corresponding to physical variables defined per unit mass are computed as

$$\theta_{\tilde{c}} = \frac{1}{m_{\tilde{c}}} \sum_k m_{\tilde{c},k} \theta_{\tilde{c},k}.$$

The update of effective pressure and sound speed is performed as described in Section 4.

7.4. Concentrations remapping

When we are modeling the multi-material flow using concentration equations, we have to remap them to consistently update the thermodynamic state of each cell. Namely, to use the multi-species EOS developed in Section 4, we need to remap the concentrations of the K fluids, from the Lagrangian grid onto the rezoned one. To this end, we first compute the mass of fluid k in the Lagrangian cell c, $m_{c,k} = \int_c \rho C_k \, dV$. We note that $m_c = \sum_{k=1}^K m_{c,k}$ since by definition $\sum_{k=1}^K C_{c,k} = 1$. Then, the mass of each fluid is conservatively interpolated onto the rezoned grid using the swept face-based method; its remapped value is referred as $m_{\tilde{c},k}$. At this point, we remark that

$$m_{\tilde{c}} \neq \sum_{k=1}^K m_{\tilde{c},k},$$

this discrepancy comes from the fact that our second-order remapping does not preserve linearity due to slope limiting. Hence, we define the new concentrations by setting $C_{\tilde{c},k} = \frac{m_{\tilde{c},k}}{m_{\tilde{c}}}$ and impose the renormalization

$$C_{\tilde{c},k} \leftarrow \frac{C_{\tilde{c},k}}{\sum_{k=1}^K C_{\tilde{c},k}}$$

so that $\sum_{k=1}^K C_{\tilde{c},k} = 1$. We point out that this necessary renormalization does not affect the global mass conservation.

8. Numerical results

All the numerical results presented in this section are performed in Cartesian geometry. The materials are characterized by a perfect gas equation of state which writes $P = (\gamma - 1)\rho\varepsilon$ where γ stands for the polytropic index of the gas. The ALE computations are performed using the relaxation procedure described in Section 6. This procedure is applied every time step.

8.1. Two-material Sod problem

We consider the two-material variant of the one-dimensional Sod shock tube problem described in [47]. As usual, the computational domain is [0,1] with an interface initially located at $x = 0.5$. The initial conditions for left material are $(\rho_l, P_l, \mathbf{U}_l, \gamma_l) = (1, 2, \mathbf{0}, 2)$ and $(\rho_r, P_r, \mathbf{U}_r, \gamma_r) = (0.125, 0.1, \mathbf{0}, 1.4)$ for the right material. We point out that this test case is a genuine two-material problems for an ALE simulation run since the polytropic index is different for the left and the right material. The initial grid is made of 100 uniform cells and the final time is $t_{\text{final}} = 0.2$. We run this problem with our multi-material ALE scheme in its Eulerian version (as Lagrange plus remap). The first computation is performed using VOF interface reconstruction and the second one uses concentration equations. The numerical results against the analytical solution are plotted in Fig. 9 for density and pressure and in Fig. 10 for velocity and internal energy. With this level of resolution, we observe a quite good agreement between the numerical and analytical solutions. As expected, the contact discontinuity obtained with the VOF interface reconstruction is sharper than the one obtained using concentration equations. We also note that the pressure plateau is very well rendered with both methods in the sense that no spurious oscillations are created at the contact discontinuity.

To see the influence of the closure model we have displayed in Figs. 11 and 12 the multi-material cell components corresponding to the previous VOF Euler computation. We notice that the partial pressures in the mixed cells has relaxed toward a common value. This relaxation is probably the consequence of the numerical diffusion by the Lagrange plus remap procedure which has been performed each time step.

Finally, in Figs. 13 and 14, we present the numerical results for the equal strain model using a VOF Lagrange computation. In this particular case, the two cells initially adjacent to interface are combined in one mixed cell. In this mixed cell, the

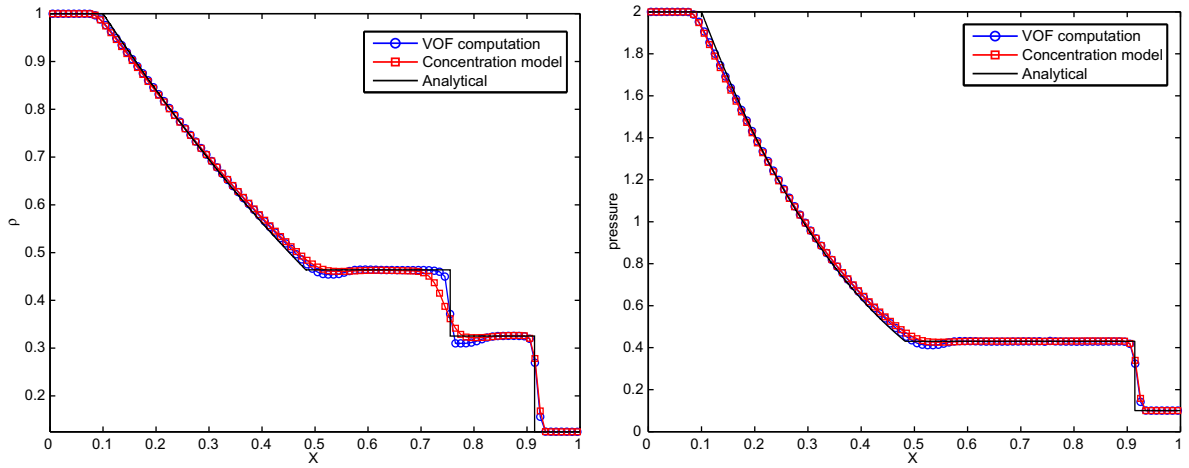

Fig. 9. Two-material Sod problem density (left) and pressure (right). VOF and concentration equations modeling versus analytical solution.

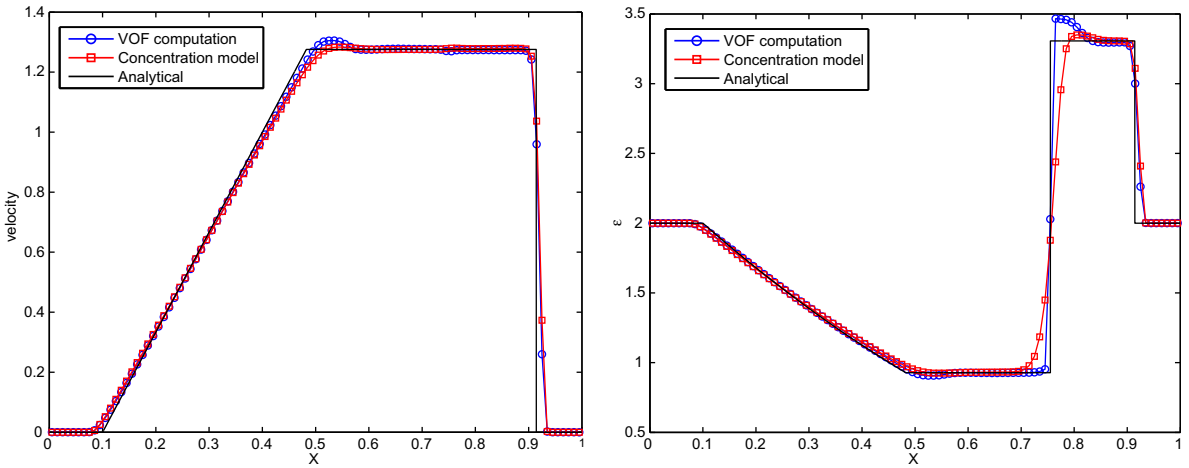

Fig. 10. Two-material Sod problem velocity (left) and internal energy (right). VOF and concentration equations modeling versus analytical solution.

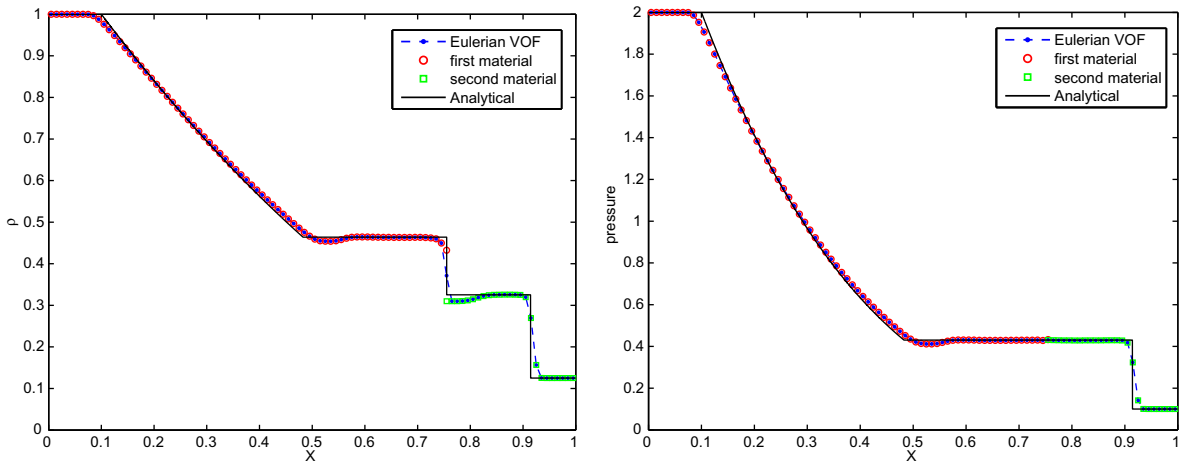

Fig. 11. Two-material Sod problem density (left) and pressure (right). VOF Euler computation versus analytical solution with multi-material cell components.

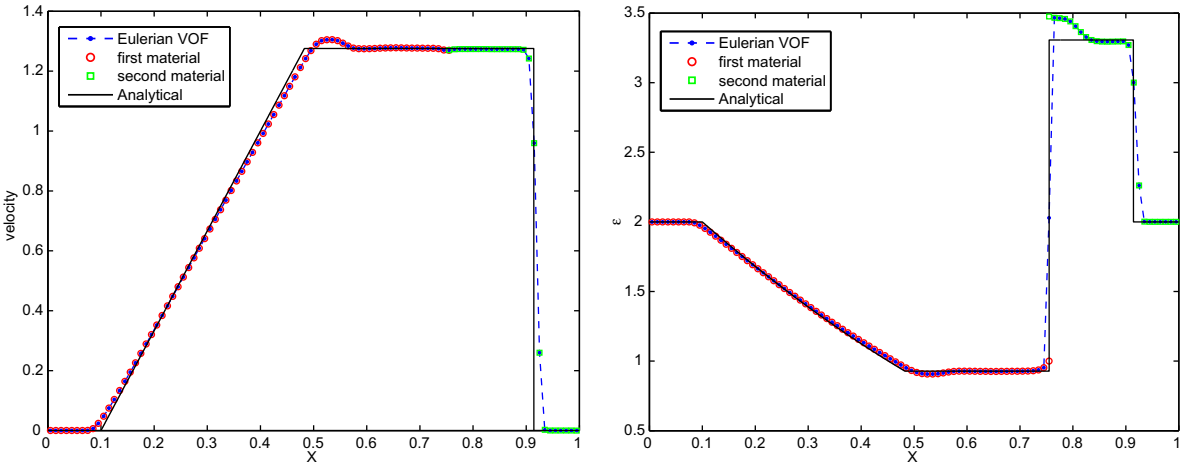

Fig. 12. Two-material Sod problem velocity (left) and internal energy (right). VOF Euler computation versus analytical solution with multi-material cell components.

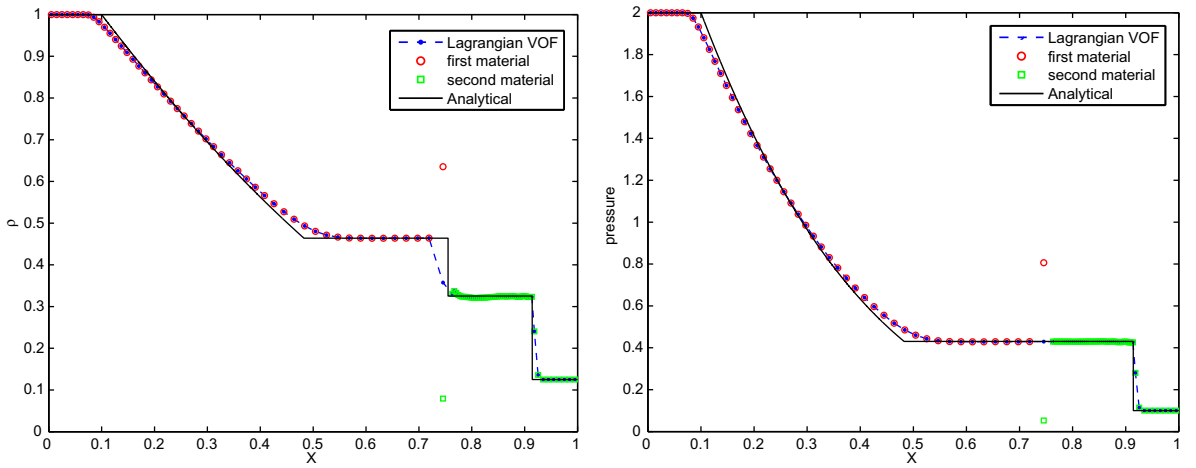

Fig. 13. Two-material Sod problem density (left) and pressure (right). VOF Lagrange computation versus analytical solution with multi-material cell components.

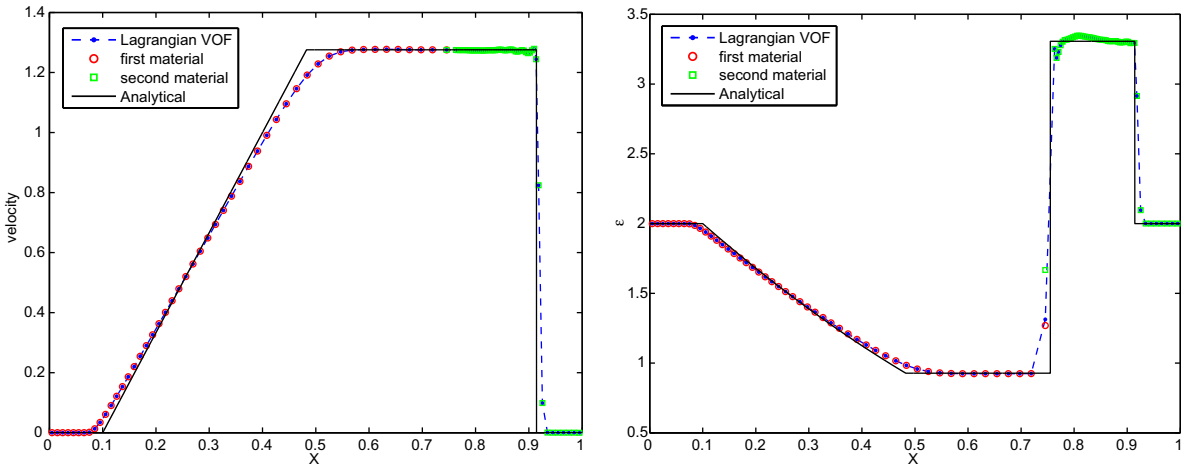

Fig. 14. Two-material Sod problem velocity (left) and internal energy (right). VOF Lagrange computation versus analytical solution with multi-material cell components.

interface is located in the middle and initial partial quantities are discontinuous. We can observe in these graphs that the partial quantities (density, pressure and internal energy) exhibit quite a large jump. This result is a direct consequence of the use of the equal strain model. This flaw can be corrected by using a more sophisticated mixed cell closure model based on pressure relaxation such as the ones presented in [4,47,24].

8.2. Sedov problem

We consider the Sedov problem for a point-blast in a uniform medium with cylindrical symmetry. An exact solution based on self-similarity arguments is available, see for instance [25]. The initial conditions are characterized by $(\rho_0, P_0, \boldsymbol{U}_0) = (1, 10^{-6}, \boldsymbol{0})$ and the polytropic index is set equal to $\frac{7}{5}$. We set an initial delta-function energy source at the origin prescribing the pressure in the cell containing the origin as follows

$$P_{\text{or}} = (\gamma - 1)\rho_{\text{or}} \frac{\mathcal{E}_0}{V_{\text{or}}},$$

where V_{or} denotes the volume of the cell that contains the origin and $\mathcal{E}_0$ is the total amount of released energy. By choosing $\mathcal{E}_0 = 0.244816$, as it is suggested in [25], the solution consists of a diverging shock whose front is located at radius $R = 1$ at

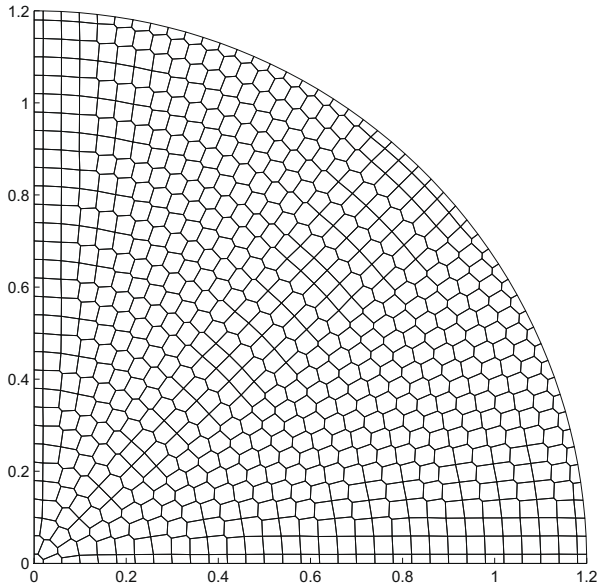

Fig. 15. Initial unstructured polygonal grid for the Sedov problem.

time $t = 1$. The peak density reaches the value 6. We point out that this simple mono-material problem does not require ALE to be run until final time. However, we use this problem as a sanity test case to demonstrate not only the accuracy and the robustness of our Lagrangian and ALE schemes but also their ability to handle real unstructured grids. We also want to assess the efficiency of the relaxation algorithm procedure. We run this problem on a unstructured grid produced by a Voronoi

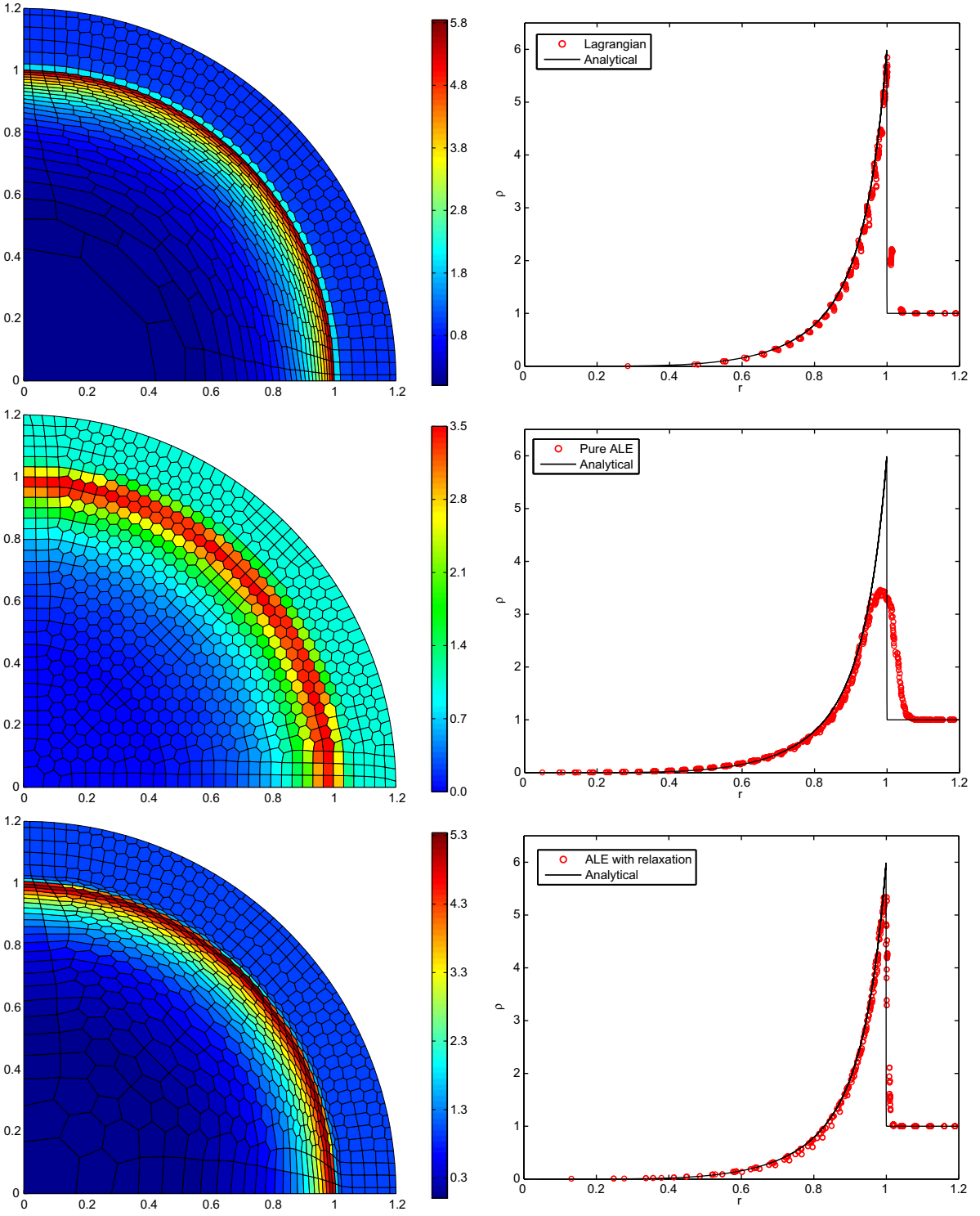

Fig. 16. Sedov problem at final time $t = 1$. From bottom to top, ALE computation with relaxation procedure, ALE computation with pure rezoning ($\omega_p = 1$) and Lagrangian computation. Left column: density map and grid, right column: density as a function of the radius of cell centers versus analytical solution.

tessellation that contains 775 polygonal cells, which is displayed in Fig. 15. Using the same initial grid, we have run a Lagrangian computation and two ALE computations. The results for the density obtained in these three configurations are displayed in Fig. 16. The Lagrangian results on top show the accuracy of the Lagrangian scheme, the shock level and its location are very well rendered. The first ALE computation (middle) has been performed switching off the relaxation procedure by setting $\omega_p = 1$, refer to Section 6. In this particular case, we note that the grid has been completely smoothed, the shock wave has been smeared over several cells and the density peak is quite far from its theoretical value. The solution is quite far from the Lagrangian solution. Moreover, we note that grid motion occurs even in regions where the flow is at rest. This flaw is visible for cells whose radius is greater than one. These remarks show the drawback of an ALE strategy using a pure rezoning phase without any relaxation procedure. The second ALE computation (bottom) has been done using our relaxation procedure in which the new grid is constructed by making a convex combination between the Lagrangian grid and the rezoned grid. This convex combination is based on the use of the ω_p factor which is evaluated using the invariant of the Cauchy–Green tensor. Using this approach, it is possible to keep the rezoned grid as close as possible to the Lagrangian grid. We observe in Fig. 16(bottom) that the results obtained with the relaxation procedure are quite close to those obtained with the Lagrangian scheme.

8.3. Triple point problem

Here, we present a two-material problem which corresponds to a three-state two-dimensional Riemann problem in a rectangular domain displayed in Fig. 17. The three-material extension of this problem using the Moment-of-Fluid method has been presented in [31]. The computational domain $\Omega = [0,7] \times [0,3]$ is split into the following three sub-domains $\Omega_1 = [0,1] \times [0,3]$, $\Omega_2 = [1,7] \times [0,1.5]$ and $\Omega_3 = [1,7] \times [1.5,3]$. The sub-domain Ω_1 contains a high-pressure high-density fluid whose initial state is $(\rho_1, P_1, \boldsymbol{U}_1) = (1,1,\boldsymbol{0})$. The sub-domain Ω_2 contains a low-pressure high-density fluid whose initial state is $(\rho_2, P_2, \boldsymbol{U}_2) = (1,0.1,\boldsymbol{0})$. The sub-domain Ω_3 contains a low-pressure low-density fluid whose initial state is

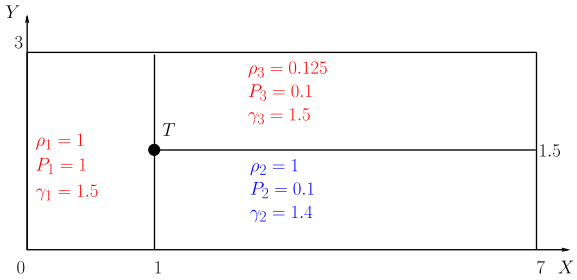

Fig. 17. Initial data for the triple point problem.

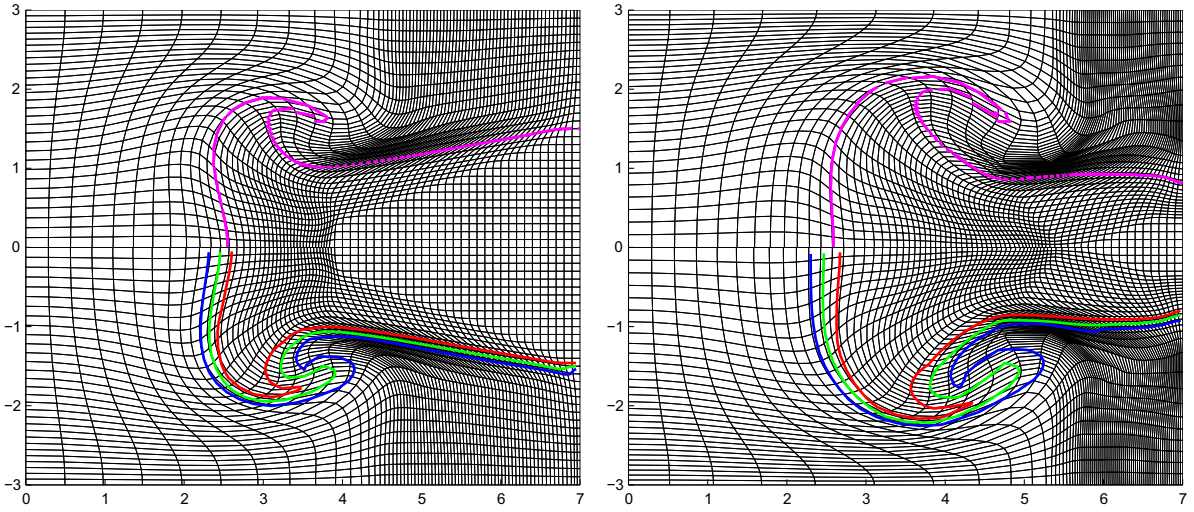

Fig. 18. Triple point problem, grid and interface at time $t = 3.5$ (left) and time $t = 5$ (right). The top part ($y > 0$) corresponds to the VOF computation and interface is the purple curve. The bottom part ($y < 0$) corresponds to the concentration equations computation, three isolines are plotted: $C = 0.1$ (blue), $C = 0.5$ (green) and $C = 0.9$ (red). (For interpretation of the references to color in this figure legend, the reader is referred to the web version of this paper.)

$(\rho_3, P_3, \boldsymbol{U}_3) = (0.125, 0.1, \mathbf{0})$. The sub-domains Ω_1 and Ω_3 are filled with the same material characterized by the polytropic index $\gamma_1 = \gamma_3 = 1.5$ whereas the sub-domain Ω_2 is filled with a different material with $\gamma_2 = 1.4$. The boundary conditions are wall boundary conditions. The final time of the simulation is $t_{\text{final}} = 5$. The initial grid is paved with 70×30 square cells.

The triple point is the point T located at the intersection of the three sub-domains Ω_1, Ω_2 and Ω_3, its coordinates are $T = (1, 1.5)^t$. Let us describe the evolution of the initial discontinuity at later time. For a point located on the interface between sub-domains Ω_1 and Ω_2, sufficiently far from the triple point T, the initial discontinuity is solved by a systems of three waves which consists of a contact discontinuity, a rightward shock wave and leftward rarefaction wave. The same situation occurs for a point located on the interface between sub-domains Ω_1 and Ω_3, sufficiently far from the triple point. We note also that the interface between sub-domains Ω_2 and Ω_3 corresponds to a contact discontinuity. In the vicinity of the triple point T the situation is more intricate, since all the aforementioned waves interact and lead to complex two-dimensional fluid flow. We point out that the two rightward shock waves in sub-domains Ω_2 and Ω_3 propagate with different speeds due to the difference of the acoustic impedance between the two fluids. Since $\rho_3 a_3 < \rho_2 a_2$, where a_2 and a_3 denotes the sound speed in sub-domains Ω_2 and Ω_3, the Ω_3 rightward shock wave propagates faster than the Ω_2 rightward shock wave. This creates a strong shear along the initial contact discontinuity located at the interface between Ω_2 and Ω_3. This shear produces a Kelvin–Helmholtz instability and a vortex formation occurs. We notice that the Lagrangian computation of this problem fails before the vortex development due to mesh tangling, refer to [34]. We run this test case using two variants of our multi-material ALE algorithm. In the first one the multi-material modeling employs the VOF interface reconstruction methodology while the second one utilizes concentration equations. Let us note that in the case of concentration equations modeling, the molar

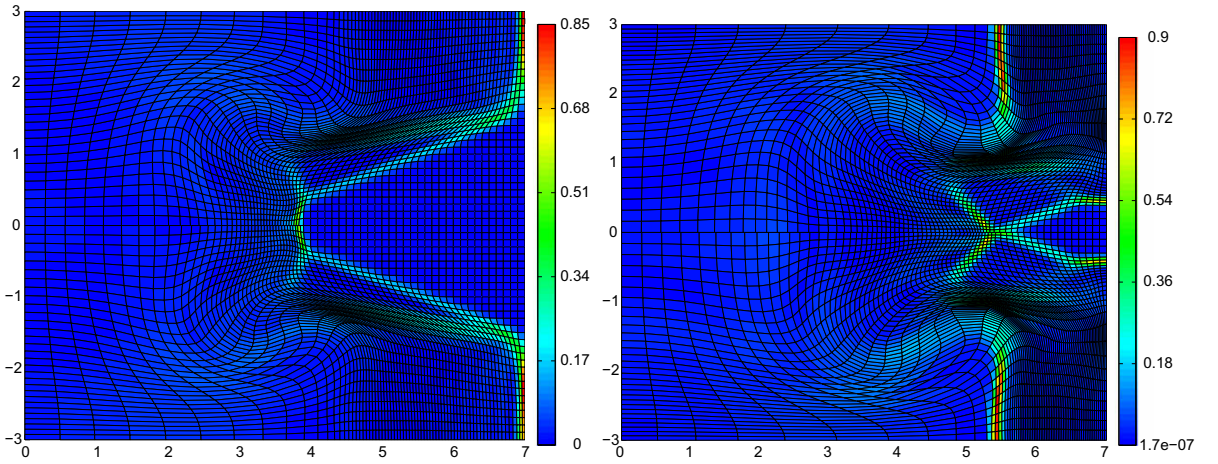

Fig. 19. Triple point problem, map of ω_p at time $t = 3.5$ (left) and time $t = 5$ (right). The top part ($y > 0$) corresponds to the VOF computation and the bottom part ($y < 0$) corresponds to the concentration equations computation.

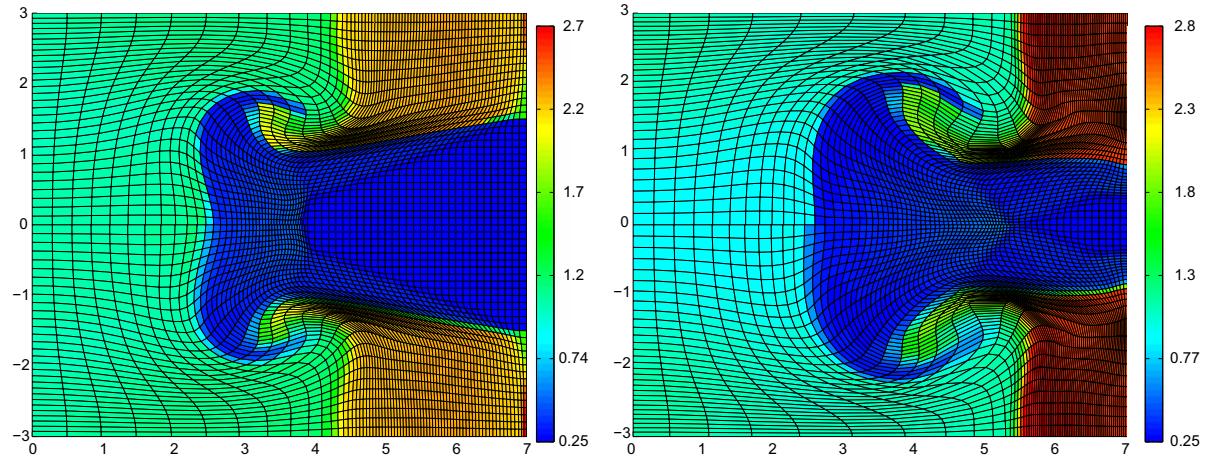

Fig. 20. Triple point problem, map of specific internal energy at time $t = 3.5$ (left) and time $t = 5$ (right). The top part ($y > 0$) corresponds to the VOF computation and the bottom part ($y < 0$) corresponds to the computation done using concentration equations.

masses of the material are set to the common value $\mathcal{M}_1 = \mathcal{M}_2 = \mathcal{M}_3 = 1$. We compare the interfaces and the grids obtained with the previous approaches in Fig. 18 before (time $t = 3.5$) and after (time $t = 5$) the fastest rightward shock wave hits the right boundary. For the VOF computation we have displayed the reconstructed interface whereas for the concentration equation modeling we have plotted three isolines which corresponds to $C = 0.1$, $C = 0.5$ and $C = 0.9$. We note a quite good agreement concerning the interface location between the two approaches. However, we observe that the interface resulting from concentration equations modeling has been diffused over several cells, leading to a numerical mixing layer, e.g. the region corresponding to $0.1 < C < 0.9$. The interface corresponding to VOF modeling has been represented by plotting segment of straight line cutting each mixed cell. As expected, it is sharper than the one obtained using concentration equations modeling. We have also displayed in Fig. 19, the ω parameter that is used in the relaxation procedure. Let us recall that this parameter is computed as a function of the eigenvalues of the Cauchy–Green tensor, refer to Section 6. The maps of ω_p are almost the same for both computations. Moreover, we remark that this parameter is a good tracer that allows to track the wave patterns. Indeed, the maxima of ω_p are concentrated in regions where strong two-dimensional compressions occur. These regions of the flow are the loci where the maximum of mesh smoothing is taken into account. Finally, to track the shock waves and the contact discontinuity we have plotted the specific internal energy map in Fig. 20. We observe quite similar results for both approaches, noticing that the vortex is little bit more diffused with the concentration equations approach.

8.4. Interaction of a shock wave with an Helium bubble

This test case corresponds to the interaction of shock wave with a cylindrical Helium bubble surrounded by air at rest [45]. The initial domain is the rectangular box $[0, L] \times \left[-\frac{h}{2}, \frac{h}{2}\right] = [0, 0.650] \times [-0.089, 0.089]$ displayed in Fig. 21. The cylindrical bubble is represented by a disk characterized by its center $(x_c, y_c) = (0.320, 0)$ and its radius $R_b = 0.025$. We prescribe wall boundary conditions at each boundary except at $x = L$, where we impose a piston-like boundary condition defined by the inward velocity $\boldsymbol{V}^\star = (u^\star, 0)$. The incident shock wave is defined by its Mach number, $M_s = 1.22$. The initial data for Helium are $(\rho_1, P_1) = (0.182, 10^5)$, its molar mass is $\mathcal{M}_1 = 5.26910^{-3}$ and its polytropic index is $\gamma_1 = 1.648$. The initial data for air are $(\rho_2, P_2) = (1, 10^5)$, its molar mass is $\mathcal{M}_2 = 28.96310^{-3}$ and its polytropic index is $\gamma_2 = 1.4$. Using the Rankine–Hugoniot relations, we find that the x-velocity of the piston is given by $u^\star = -124.824$. The x-component of the incident shock velocity is $D_c = -456.482$. The incident shock wave hits the bubble at time $t_i = 668.153 \times 10^{-6}$. The stopping time for our computation is

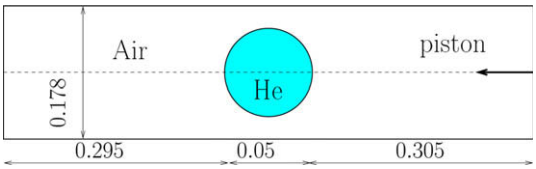

Fig. 21. Interaction of a shock wave with an Helium bubble. Geometry of the computational domain.

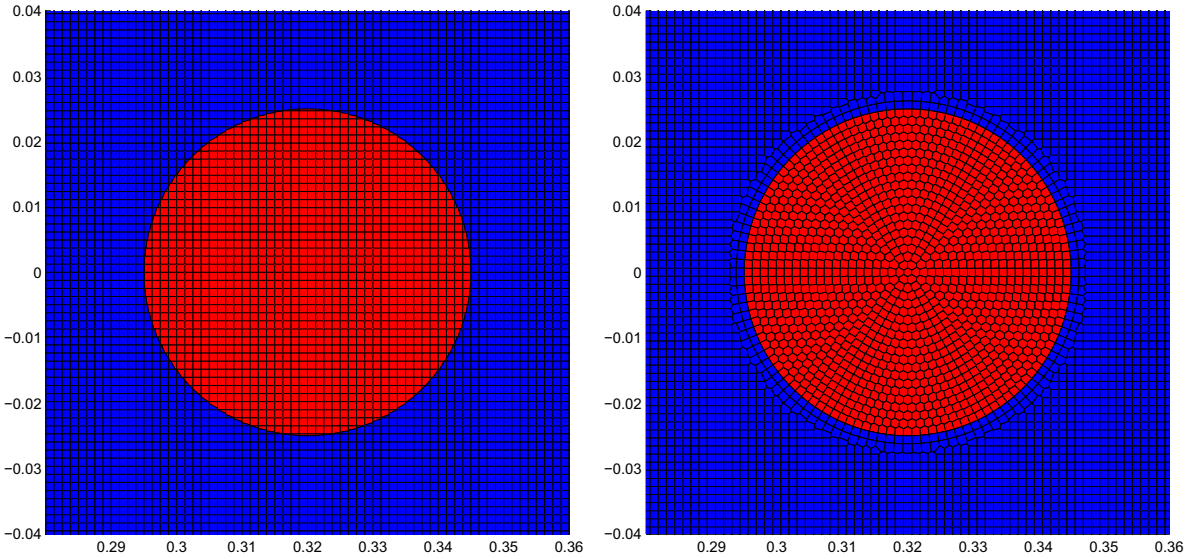

Fig. 22. Interaction of a shock wave with an Helium bubble. Zoom on the initial grid in the vicinity of the bubble and color map of volume fraction. Cartesian grid (left) and polygonal unstructured grid (right).

$t_{final} = t_i + 674 \times 10^{-6} = 1342.153 \times 10^{-6}$. It corresponds to the time for which experimental shadow-graph extracted from [21] is displayed in [45].

To compute this problem, we have constructed two grids. The first one is a Cartesian grid that contains $520 \times 144 = 74{,}880$ square cells. In this case, the initialization of the volume fraction is performed by computing the intersection between the circle, which corresponds to the bubble boundary, and the Cartesian grid. Thus, we create mixed cells wherein the interface is represented by segment of straight line. The second grid is a polygonal grid that results from a Voronoi tessellation wherein the boundary of the bubble is represented by faces of polygonal Voronoi cells, refer to [34] for more details about the construction of such a grid. This polygonal grid contains 75,507 cells which is approximately the same number of cells than the Cartesian grid. We note that this initial polygonal grid does not contain any mixed cells. We have displayed these grids in Fig. 22.

We have performed computations using VOF modeling for both grids with same grid relaxation procedure. We have displayed in Fig. 24 for both grids the time evolution of the bubble. The first snapshot, located at the top of the figure, corresponds to time $t = 800 \times 10^{-6}$, after the interaction of the shock wave with the bubble. This interaction of the planar leftward shock wave with the curved bubble interface leads to a transmitted shock and vortices formation. A complex system of waves interaction takes place, refer to [45] for a detailed analysis. At later times, $t = 1100 \times 10^{-6}$ (middle) and

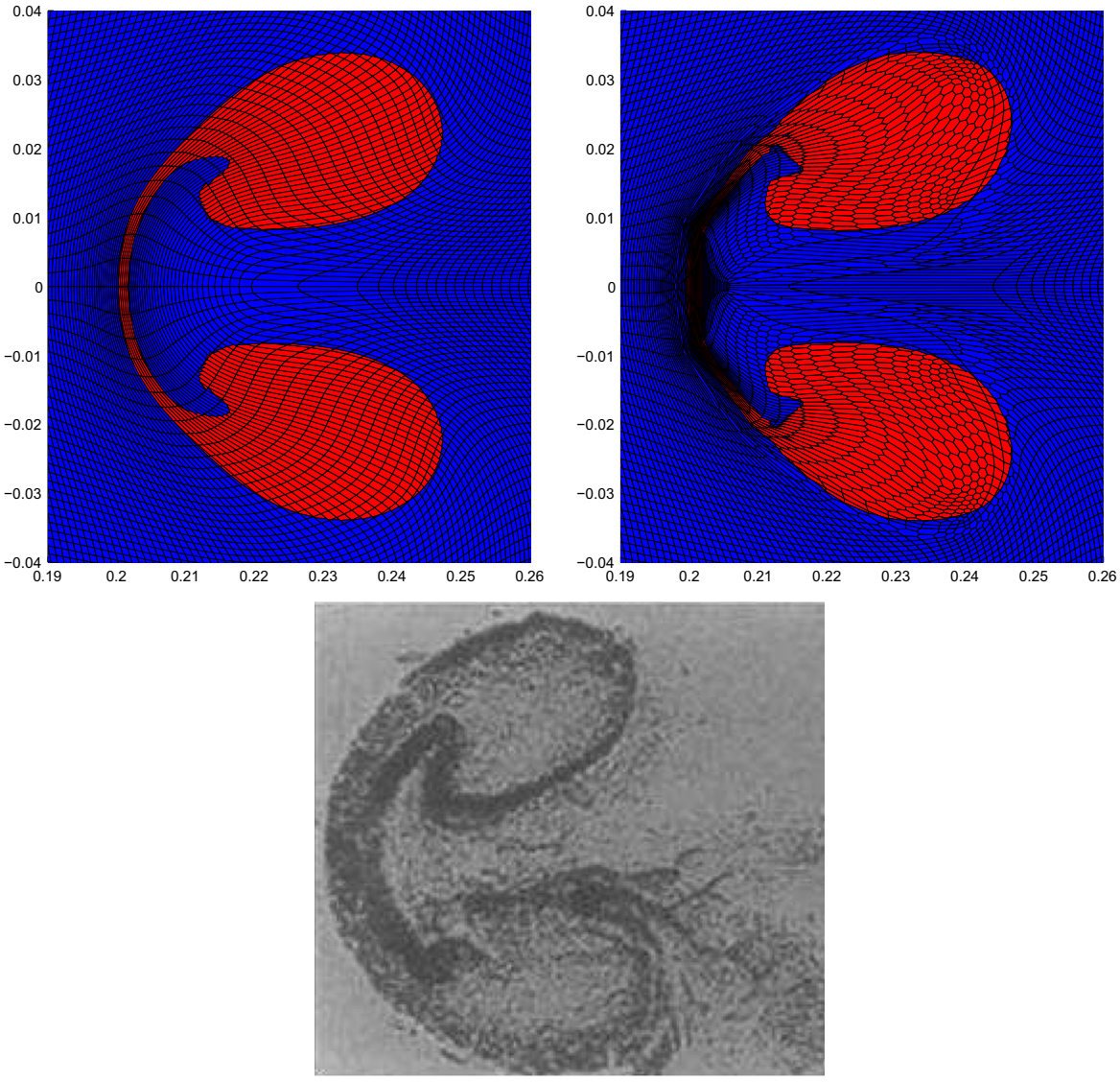

Fig. 23. Interaction of a shock wave with an Helium bubble. Zoom on the bubble at $t_{final} = 1342.153 \times 10^{-6}$ and color map of volume fraction. Cartesian grid on top left, polygonal grid on top right versus Schlieren image from experimental data [21] (bottom).

$t = 1342.153 \times 10^{-6}$ (bottom) the shape of bubble is strongly distorted. We note that the results obtained with both grids are quite similar. The comparison of an experimental Schlieren image [21] and the numerical results at the final time has been displayed in Fig. 23. It reveals a good agreement that validates our ALE strategy from a qualitative point of view. It remains to perform a quantitative validation using the numerical and experimental results presented in [45]. This will be the topics of a future paper. Finally, to illustrate the relevancy of our relaxation parameter ω_p, we have plotted it in Fig. 25, on a twice finer Cartesian grid at time $t = 800 \times 10^{-6}$. We clearly see not only the fine structures of the interacting waves but also the shape of the bubble. This ω_p factor turns out to be a very relevant parameter to capture accurately the waves of the fluid flow.

8.5. Incompressible Rayleigh–Taylor instability

This test case deals with the well-known incompressible Rayleigh–Taylor instability. The computational domain is the rectangular box $[0, \frac{1}{3}] \times [0, 1]$ which is paved with 34×100 cells. The initial set up consists of two immiscible fluids which are separated by a perturbed interface, whose equation writes $y_i(x) = \frac{1}{2} + a_0 \cos(6\pi x)$. The interface amplitude a_0 is set to the value $a_0 = 10^{-2}$. The heavy fluid is located above the light one. The densities of the two fluids are $\rho_h = 2$ and $\rho_l = 1$. The same polytropic index $\gamma_h = \gamma_l = 1.4$ is shared by the two fluids. A downward gravity field is applied, $\boldsymbol{g} = (g_x, g_y)^t = (0, -0.1)^t$. Initially both fluids are at rest and the initial pressure distribution is deduced by setting hydrostatic equilibrium as

$$P_h(x,y) = 1 + \rho_h g_y (y - 1), \quad \text{if } y > y_i(x),$$
$$P_l(x,y) = 1 + \rho_h g_y [y_i(x) - 1] + \rho_l g_y [y - y_i(x)], \quad \text{if } y \leqslant y_i(x).$$

It is well known that this configuration is unstable and as time evolves, the heavy fluid will sink while the light fluid will rise. Due to the sinusoidal interface, vortices develop in the vicinity of the interface and lead at later time to an interface which has a mushroom-like shape. Although this problem is incompressible and does not involve any shock wave, we run it using

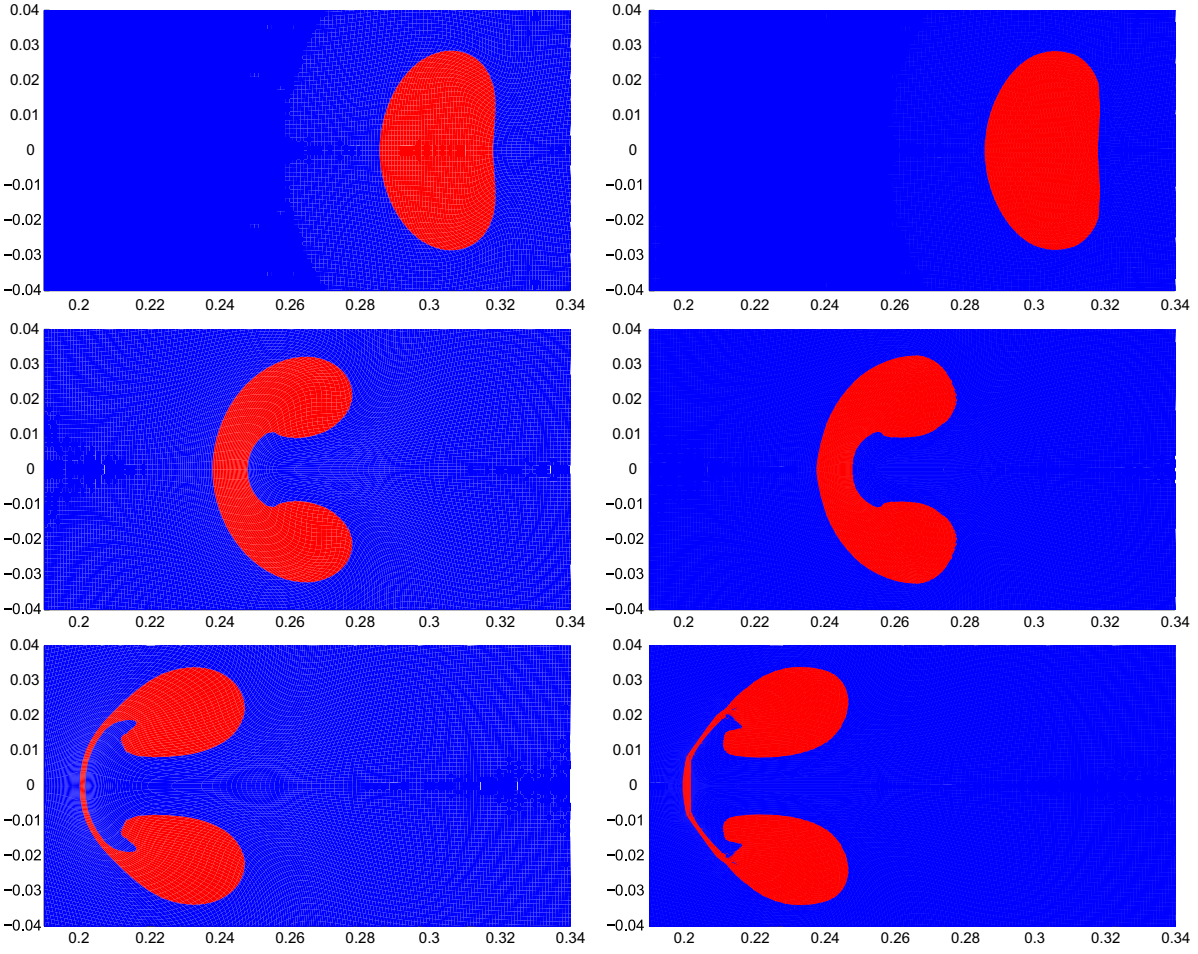

Fig. 24. Interaction of a shock wave with an Helium bubble. Map of the volume fraction in the vicinity of the bubble. Cartesian grid (left) and polygonal grid (right). From top to bottom, snapshots at $t = 800 \times 10^{-6}$, $t = 1100 \times 10^{-6}$ and $t = 1342.153 \times 10^{-6}$.

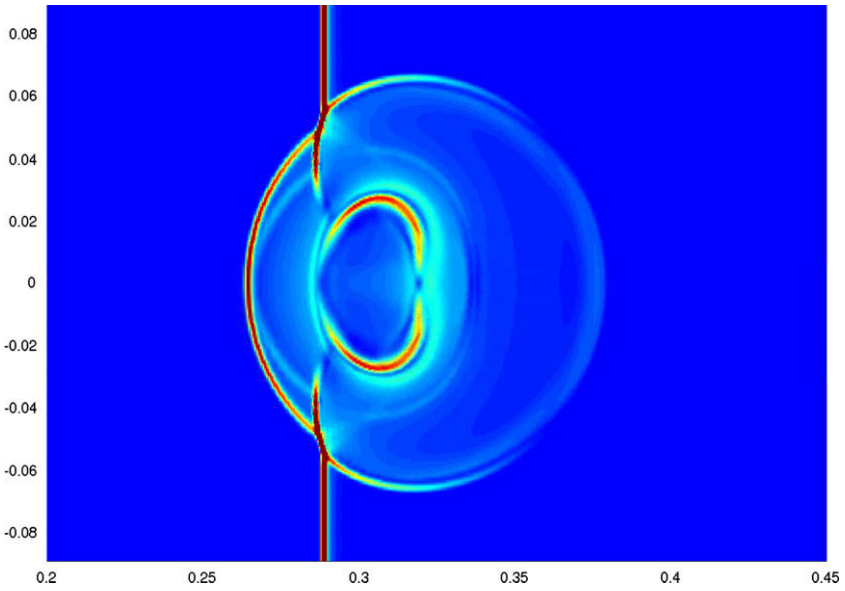

Fig. 25. Interaction of a shock wave with an Helium bubble. Map of ω_p parameter in the vicinity of the bubble for a twice finer Cartesian grid at $t = 800 \times 10^{-6}$. The red color indicates the maximum value, i.e. it shows the regions where the maximum deformation occurs. (For interpretation of the references to color in this figure legend, the reader is referred to the web version of this paper.)

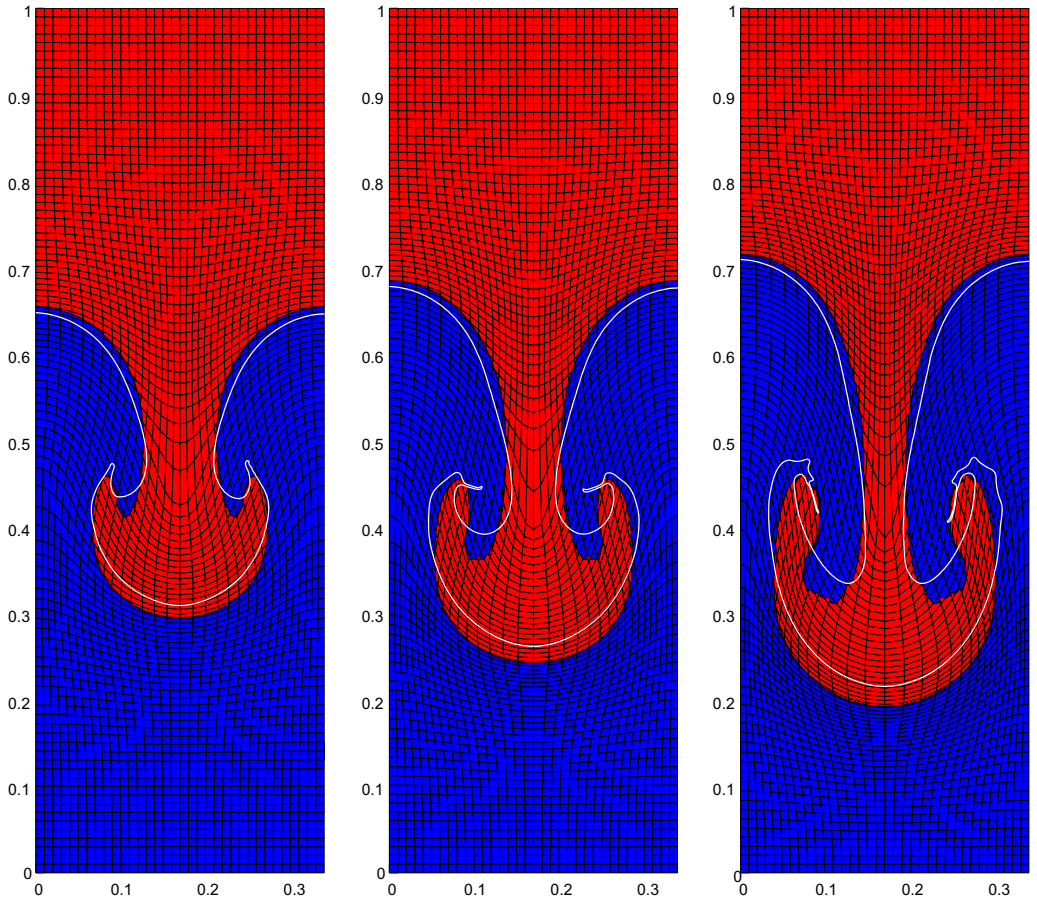

Fig. 26. Incompressible Rayleigh–Taylor instability. Snapshots of the grid and map of the volume fraction at times $t = 7$, $t = 8$ and $t = 9$ versus FronTier interface (white curve).

our multi-material compressible ALE algorithm using VOF modeling. The initial volume fractions are computed by performing the intersection of the sinusoidal interface with the Cartesian grid. The computation is run until the final time $t_{\text{final}} = 9$. We have plotted in Fig. 26 the grid and interface at times $t = 7$, $t = 8$ and $t = 9$. We have also superimposed the interface obtained using the front tracking code FronTier [20,19]. The results of this code are used by the courtesy of J.W. Grove of the Los Alamos National Laboratory. We point out that FronTier is run with a very fine resolution characterized by 106×320 cells. We note a rather good agreement between our results and Frontier interface which shows the ability of our compressible ALE method to handle incompressible flows wherein strong vorticity occurs.

8.6. Multi-mode implosion in cylindrical geometry

The aim of this test case is to assess the capability of our multi-material ALE algorithm to handle a multi-mode implosion in cylindrical geometry. This test problem which has been initially proposed in [52] is quite close to a real-life problem such as that encountered in Inertial Confinement Fusion (ICF) simulation. At the beginning of the problem, a cylinder of light fluid ($R \in [0,1]$) is surrounded by a shell of dense fluid ($R \in [1,1.2]$), refer to Fig. 27. For both fluids the polytropic index is $\gamma_l = \gamma_h = \frac{5}{3}$. The initial densities and pressures are $(\rho_l, P_l) = (0.05, 0.1)$ and $(\rho_h, P_h) = (1, 0.1)$. The implosion is driven by prescribing the following pressure law on the outside of the dense shell

$$P^\star(t) = \begin{cases} 13, & \text{if } t \in [0; 0.04], \\ 13 - 12.5\frac{t-0.04}{0.125-0.04}, & \text{if } t \in [0.04; 0.125], \\ 0.5, & \text{if } t \in [0.125; 0.3]. \end{cases} \tag{36}$$

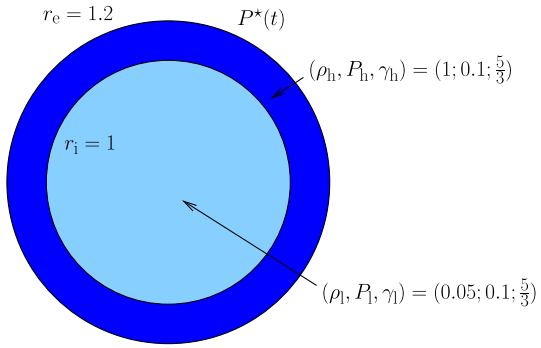

Fig. 27. One-dimensional implosion. Initial geometry and data.

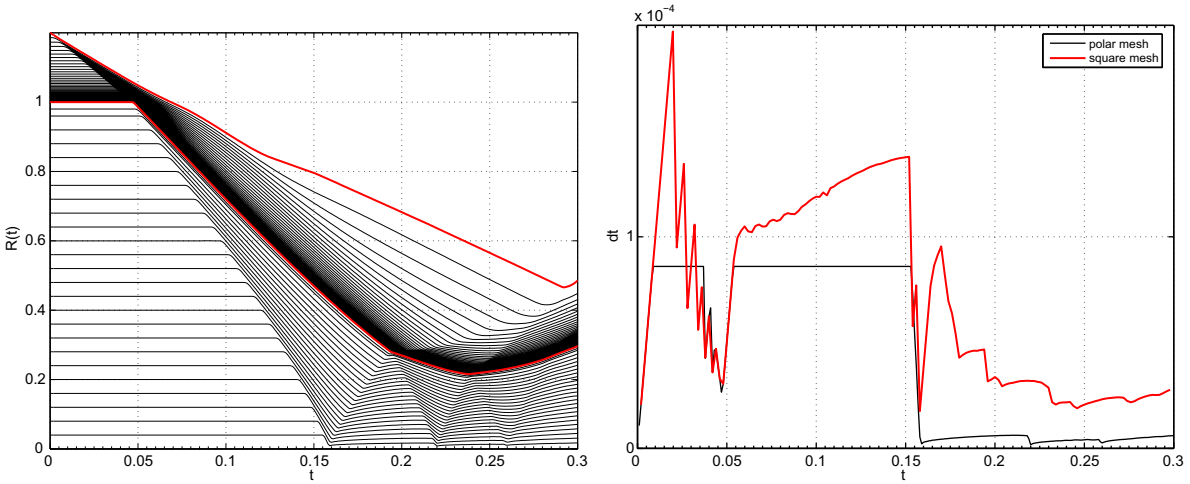

Fig. 28. t–R diagram for the one-dimensional implosion (left). Time step history for the one-dimensional implosion using two-dimensional grids (right). The black curve corresponds to the polar grid while the red one refers to the unstructured grid. (For interpretation of the references to color in this figure legend, the reader is referred to the web version of this paper.)

We separate our study in two parts. The first one is devoted to the study of the one-dimensional implosion using two-dimensional grids. The second one consists in investigating the development of hydrodynamic instabilities which result from an initial multi-mode perturbation of the interface between the light and heavy fluid.

8.6.1. One-dimensional implosion

The time history of the pressure driven implosion is displayed in Fig. 28(left), using a classical t–R diagram. This diagram is based on a one-dimensional Lagrangian computation. The one-dimensional grid is done using 50 equal size cells in the light fluid and 40 non-equal size cells in the heavy fluid. The cells in the heavy fluid are graded according to a geometric progression to obtain a mass matching grid at the interface. The t–R diagram consists in plotting the radius of each point of the grid as function of time. We have also plotted the outer and the inner radii using thick red curves. This t–R diagram allows to visualize the waves that are present in the flow. We clearly observe the consecutive bounces of the shock waves at the center that leads to a deceleration of the shell and the so-called stagnation phase wherein the inner interface radius reaches its minimum value. After this phase, the flow becomes Rayleigh–Taylor unstable, that is if the inner interface is initially perturbed, this perturbation will grow exponentially as function of time. This instability is due to the fact that the light

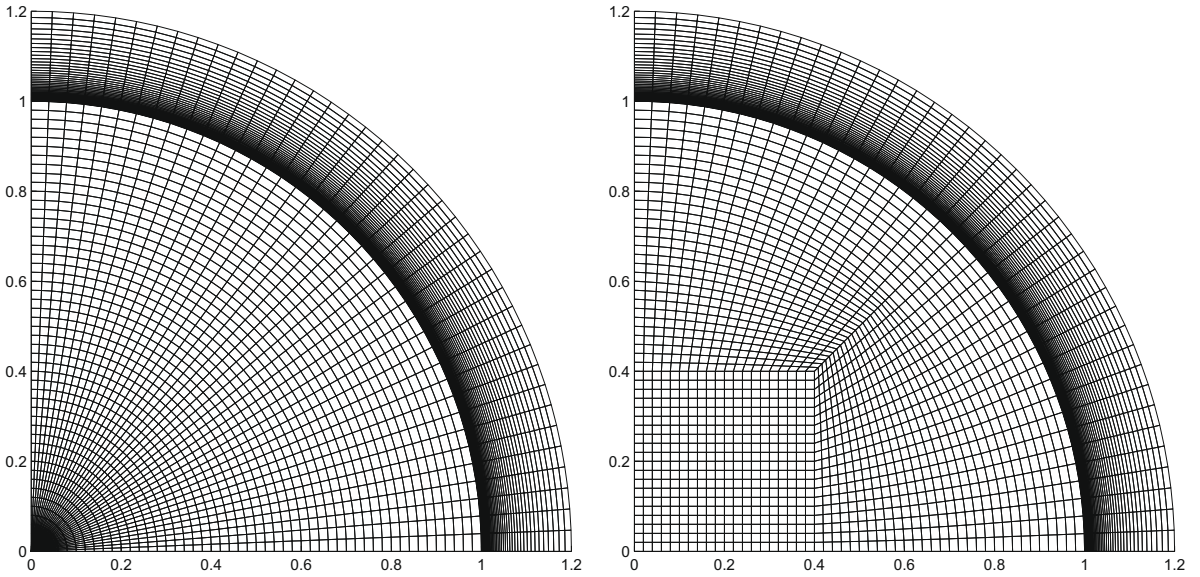

Fig. 29. Initial grids for the one-dimensional implosion. Polar grid (left) and unstructured grid (right).

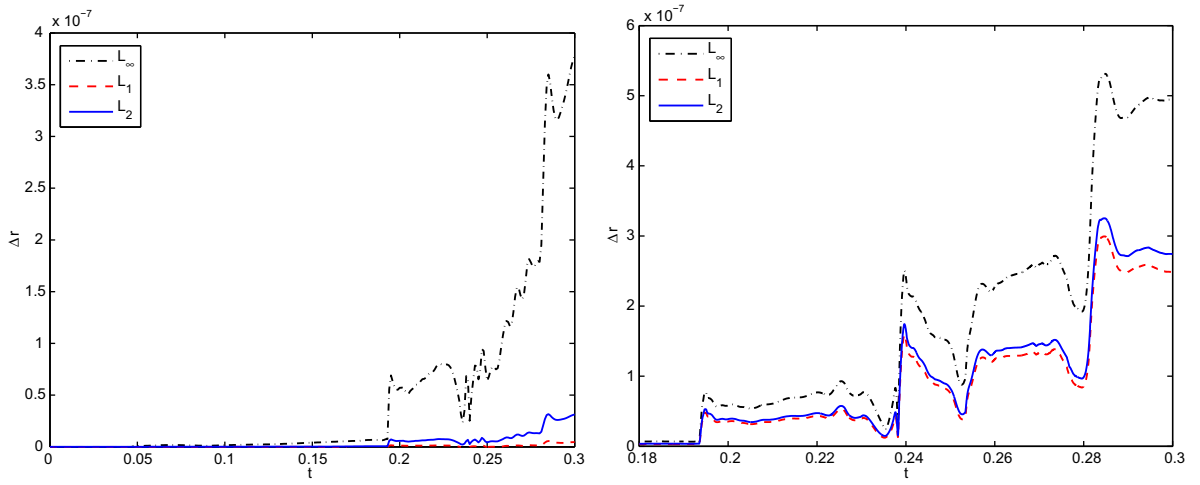

Fig. 30. One-dimensional cylindrical implosion. Symmetry preservation indicators using a two-dimensional polar grid. Lagrangian computation (left) versus multi-material ALE computation using VOF modeling (right).

fluid is pushing the heavy fluid during the deceleration phase. We also point out that in case of an initially perturbed interface we would also have encountered Richtmyer–Meshkov instability due to shock wave that crosses the inner interface. This Richtmyer–Meshkov instability is characterized by a linear growth rate in time for the amplitude perturbations and thus is less dangerous that the Rayleigh–Taylor instability. The interesting reader should refer to [33] for more details about these hydrodynamics instabilities an their links with ICF target design. To assess the robustness and the accuracy of our multi-material ALE scheme using VOF modeling we have performed computations with unperturbed interface using two kinds of two-dimensional grids. The first one is a polar grid which is displayed in Fig. 29(left). This grid contains 90×40 cells and is characterized by a mass matching radial spacing which is similar to the aforementioned one-dimensional Lagrangian grid. The other grid, displayed in Fig. 29(right), is an unstructured one that contains 3200 cells. We point out that this grid is made of three structured quadrangular zones paved with quadrangular cells. The junction of these three zones is a triple point, that is an exceptional vertex surrounded by three cells. For both grids, we prescribe symmetry boundary conditions on the x- and y-axis, and the one-dimensional pressure law given by (36) on the outer boundary. The advantage of using an unstructured grid lies in the fact that it allows a less constrained time step, refer to Fig. 28(right). The time step for the polar grid is smaller due to the high aspect ratio triangular elements near the origin. An important issue for the simulation of Rayleigh–Taylor unstable flows of this type is the preservation of symmetry.

In order to quantify how well symmetry is preserved the following metrics are proposed

$$L_\infty(t) = \max_{i=1,\dots,41} |r_i(t) - \bar{r}(t)|,$$

$$L_1(t) = \frac{1}{41}\sum_{i=1}^{41} |r_i(t) - \bar{r}(t)|,$$

$$L_2(t) = \sqrt{\frac{1}{41}\sum_{i=1}^{41} [r_i(t) - \bar{r}(t)]^2}.$$

Here, $r_i(t)$ denotes the radius of a vertex located on the interface and $\bar{r}(t)$ is the mean value of the interface radius computed according to

$$\bar{r}(t) = \frac{1}{41}\sum_{i=1}^{41} r_i(t).$$

We have displayed in Fig. 30, these symmetry preservation indicators corresponding to a Lagrangian (left) and a multi-material ALE VOF (right) computations using the polar grid. As expected the Lagrangian computation is correct since the maximum deviation from symmetry preservation is around 4×10^{-7}, which is a rather satisfying value. The values for the multi-material ALE VOF computation are a little bit bigger but remain still acceptable. We have also plotted the corresponding indicators in the case of the unstructured grid. For the Lagrangian computation, refer to Fig. 31(left), the maximum of symmetry preservation deviation is around 4×10^{-4}. This higher value is due to the non-symmetry of the initial unstructured grid. We observe that for the multi-material ALE VOF computation, refer to Fig. 31(right), the symmetry preservation indicator grows to 1.5×10^{-3}. We conclude that the symmetry preservation capability of our multi-material ALE VOF algorithm interface is directly comparable to the one of the Lagrangian method, which can be considered as a reference.

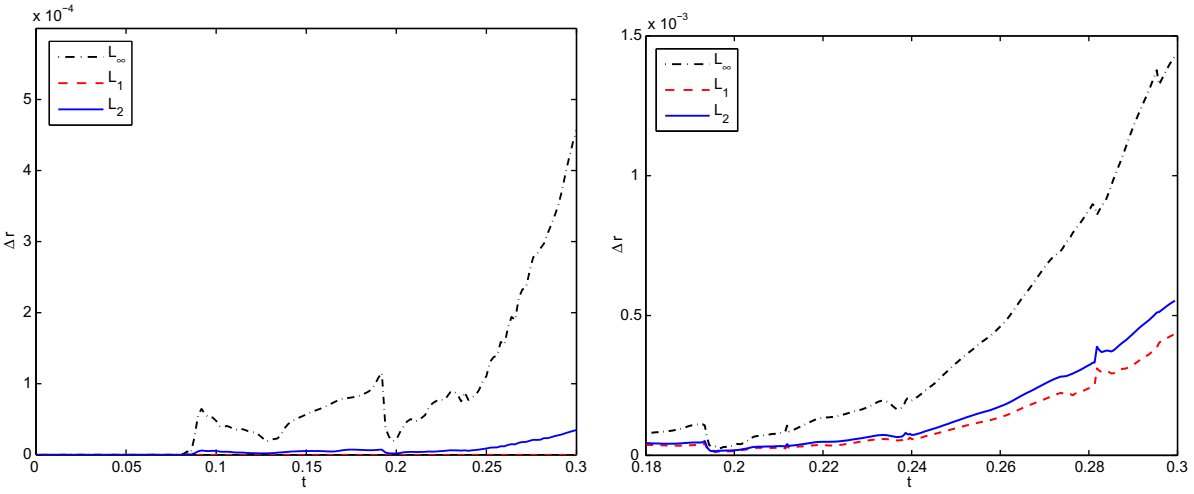

Fig. 31. One-dimensional cylindrical implosion. Symmetry preservation indicators using a two-dimensional unstructured grid. Lagrangian computation (left) versus multi-material ALE computation using VOF modeling (right).

The non-symmetric unstructured grid is clearly less stable than the polar grid. However, we point out that we do not introduce spurious unstable modes that could appear during the exponential growth of the Rayleigh–Taylor instability, refer to Fig. 32 where we have displayed both grids at the final computation time.

8.7. Two-dimensional implosion with perturbed interface

After investigating the capability of symmetry preservation of our multi-material ALE scheme, we are now ready to study the development of a compressible Rayleigh–Taylor instability. To this end, we prescribe an initial perturbation at the interface between light and heavy fluid in the following manner

$$r_i^{\text{pert}} = r_i[1 + a_0 \cos(n\theta)].$$

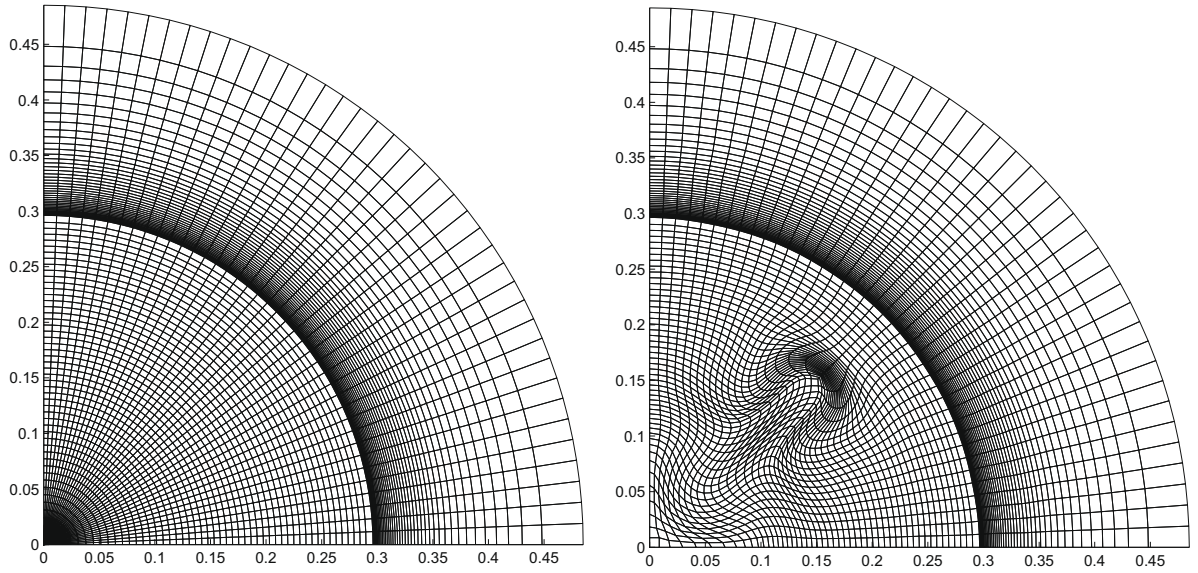

Fig. 32. One-dimensional cylindrical implosion. Grids at final time for the multi-material ALE computation using VOF modeling. Polar grid (left) and unstructured grid (right).

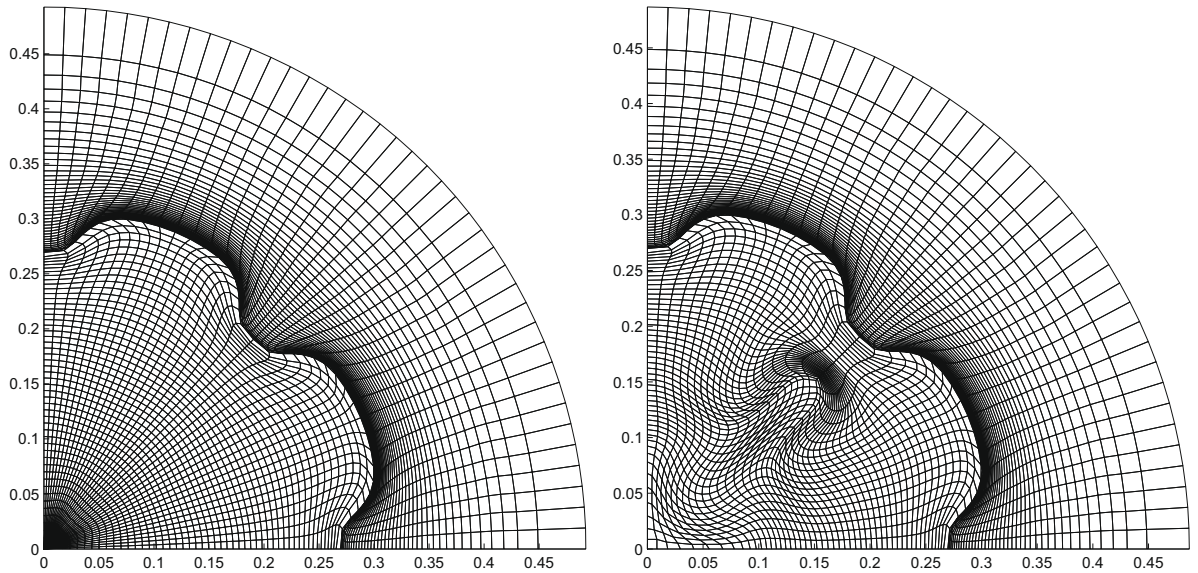

Fig. 33. Two-dimensional implosion with perturbed interface. Lagrangian computation with $a_0 = 2 \times 10^{-4}$. Grids at final time, $t = 0.3$, corresponding to the initial polar grid (left) and the initial unstructured (right).

Here, r_i and r_i^{pert} denote the unperturbed and perturbed radii, a_0 is the amplitude of the perturbation and the integer n corresponds to the mode of the perturbation. We compute this problem using the aforementioned two-dimensional grids for two different initial amplitudes $a_0 = 2 \times 10^{-4}$ and $a_0 = 10^{-3}$ with the same mode $n = 8$.

The Lagrangian computations with $a_0 = 2 \times 10^{-4}$ are displayed in Fig. 33 at the final time $t = 0.3$. We note that final grids remain valid for both initial grids. The Lagrangian computations corresponding to $a_0 = 10^{-3}$ fails at $t_{\text{fail}} = 0.24$ for both grids due to mesh tangling, refer to Fig. 34. This is not a surprise, as the higher the initial amplitude, the stronger the development of the Rayleigh–Taylor instability.

Finally, we perform multi-material ALE VOF computations of this two-dimensional implosion with perturbed interface. The final grids and the interfaces for the initial amplitude $a_0 = 2 \times 10^{-4}$ are plotted in Fig. 35. We observe that the development of the instability is quite similar for both grids and moreover is comparable to what has been obtained using

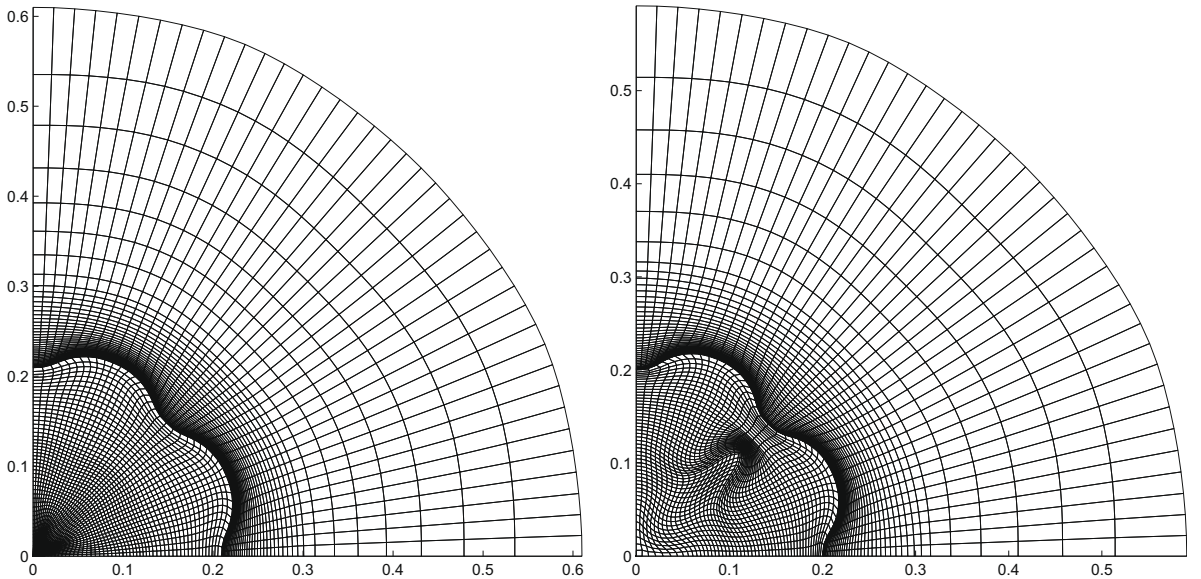

Fig. 34. Two-dimensional implosion with perturbed interface. Lagrangian computation with $a_0 = 10^{-3}$. Grids at failure time, $t_{\text{fail}} = 0.24$, corresponding to the initial polar grid (left) and the initial unstructured (right).

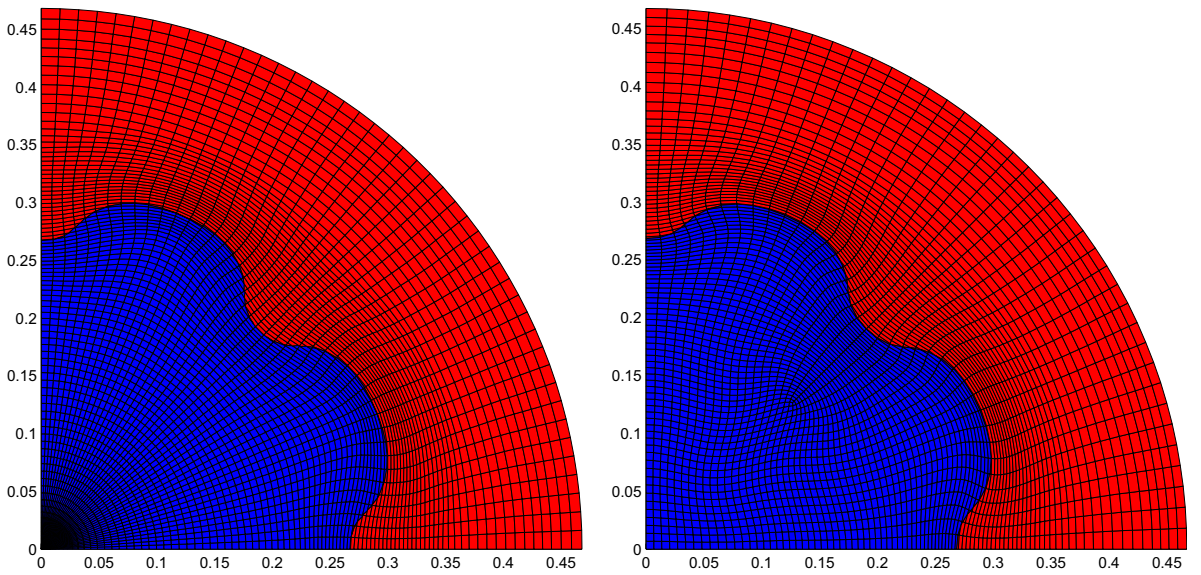

Fig. 35. Two-dimensional implosion with perturbed interface $a_0 = 2 \times 10^{-4}$. Grids and interfaces at the final time, $t = 0.3$, corresponding to the initial polar grid (left) and the initial unstructured grid (right).

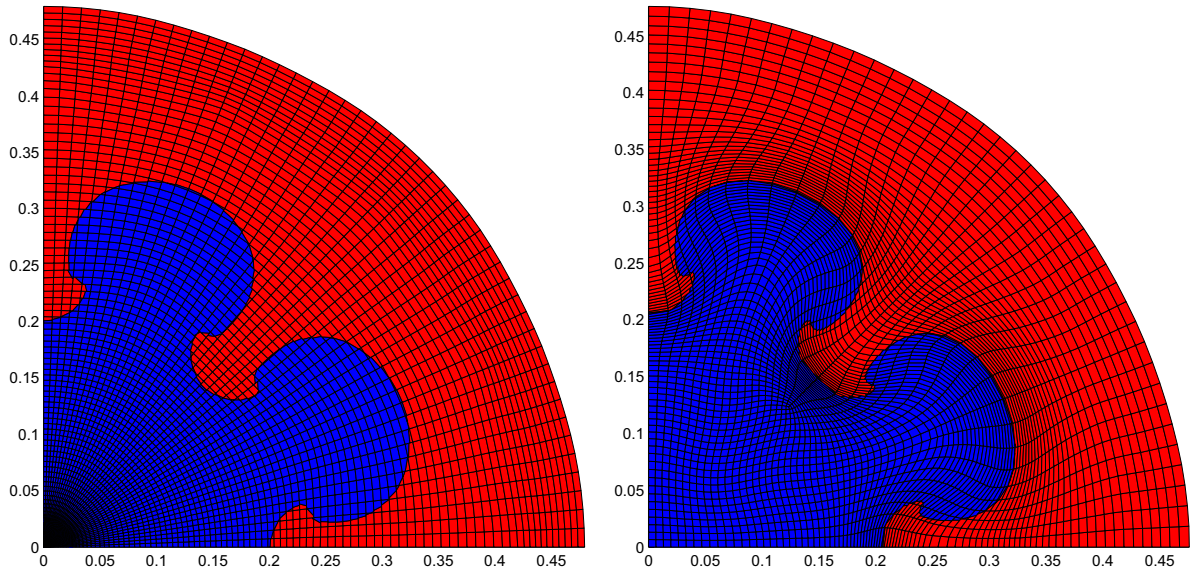

Fig. 36. Two-dimensional implosion with perturbed interface $a_0 = 10^{-3}$. Grids and interfaces at the final time, $t = 0.3$, corresponding to the initial polar grid (left) and the initial unstructured grid (right).

Lagrangian computations, refer to Fig. 33. Using the same framework, we have displayed the results obtained for the initial amplitude $a_0 = 10^{-3}$. Contrary to the Lagrangian computations, the multi-material ALE computations run without any problem up to the final time. We can observe, in Fig. 36, the same development of the interface instability for both initial grids. We also note that the time step corresponding to the initial unstructured grid is much higher than the one corresponding to the initial polar grid, thus leading to a total computational time for the unstructured grid which is ten times smaller.

Comment 4. We point out that nothing has been done to optimize the quality of the reduced connectivity mesh. We assume that some initial pre-smoothing of the reduced connectivity grid would probably improve symmetry preservation and decrease the jet appearing at 45°.

9. Conclusion

We have described a new high-order cell-centered ALE discretization devoted to the numerical simulation of two-dimensional multi-material compressible fluid flows on general polygonal grids with fixed topology. Our ALE algorithm includes the three following phases:

- An explicit Lagrangian phase wherein physical variables and the unstructured grid are updated by means of a recent cell-centered high-order Lagrangian scheme [37].
- An original rezoning phase in which the rezoned grid is defined as a convex combination between the regularized grid and the Lagrangian grid. This convex combination is constructed through the use of an ω factor which is expressed in terms of the invariants of the right Cauchy–Green tensor with respect to the Lagrangian displacement over a time step. This relaxation procedure is Galilean invariant and allows to keep the rezoned grid as close as possible to the Lagrangian grid.
- A remapping phase in which physical variables are conservatively interpolated from the Lagrangian grid onto the rezoned one.

Regarding the thermodynamical closure for multi-material flows, we have presented two different approaches. The first one, which corresponds to the case of miscible fluids, employs concentration equations and a mixture EOS derived by assuming pressure–temperature equilibrium. The second one, which corresponds to the case of immiscible fluids utilizes the Volume Of Fluid methodology and allows a Lagrangian tracking capability for material interfaces in our ALE algorithm. In this particular approach, the mixed cell closure is obtained by means of the equal strain assumption. The numerical results that have been displayed demonstrate the accuracy and the robustness of our ALE methodology in comparison to purely Lagrangian discretization.

At this point, we acknowledge that our ALE implementation is far from being optimal from the point of view of its capability, accuracy and efficiency. Concerning its capability and accuracy, we plan to improve the multi-material modeling in the

case of immiscible fluids by implementing the Moment Of Fluid algorithm [2,16]. This enhancement will allow to take into account more than two-materials and to reconstruct interfaces with a higher order of accuracy. We also plan to investigate the implementation of more sophisticated mixed cell closure models such as pressure relaxation models [4,24]. Concerning its efficiency, we intend to improve the remapping phase replacing the costly exact intersection remapping algorithm by an hybrid remapping phase which is a combination of the swept face-based and cell-intersection-based methods. In this hybrid remapping approach the use of exact intersection remapping will be restricted to a buffer layer located in the vicinity of the interfaces between materials. This hybrid method will be described in a forthcoming paper [18]. We also intend to improve our grid relaxation procedure. First, we think that it is possible to enhance the smoothing algorithm by incorporating some physical weight into it. Second, we plan to include more physics into the ω parameter definition to better take into account shear and vorticity using the polar decomposition of the right Cauchy–Green tensor [27]. Finally, to demonstrate the ability of our method on more realistic problems, in a next paper, we will provide its two-dimensional extension to axisymmetric geometry.

Acknowledgments

The authors thank M. Kucharik, R. Liska, R. Loubère, B. Rebourcet, M. Shashkov and P. Vachal for many fruitful and stimulating discussions about Lagrangian hydrodynamics and multi-material ALE. The authors are also grateful to J. Grove from the Los Alamos National Laboratory for providing us the Frontier results and allowing their use.

References

[1] F.L. Adessio, D.E. Carroll, K.K. Dukowicz, J.N. Johnson, B.A. Kashiwa, M.E. Maltrud, H.M. Ruppel, Caveat: a computer code for fluid dynamics problems with large distortion and internal slip, Technical Report LA-10613-MS, Los Alamos National Laboratory, 1986.
[2] H.T. Ahn, M.J. Shashkov, Multi-material interface reconstruction on generalized polyhedral meshes, J. Comput. Phys. 226 (2) (2007) 2096–2132.
[3] H.R. Anbarlooei, K. Mazaheri, Moment of fluid interface reconstruction method in multi-material arbitrary Lagrangian–Eulerian (MMALE) algorithms, Comput. Methods Appl. Mech. Eng. 198 (2009) 3782–3794.
[4] A. Barlow, A new Lagrangian scheme for multimaterial cells, in: Proceedings of European Congress on Computational Methods in Applied Sciences and Engineering, ECCOMAS Computational Fluid Dynamics Conference, Swansea, Wales, 2001, pp. 262–297.
[5] A.J. Barlow, A compatible finite element multi-material ALE hydrodynamics algorithm, Int. J. Numer. Meth. Fluids 56 (8) (2008) 953–964.
[6] T.J. Barth, D.C. Jespersen, The design and application of upwind schemes on unstructured meshes, in: AIAA paper 89-0366, 27th Aerospace Sciences Meeting, Reno, Nevada, 1989.
[7] M. Ben-Artzi, J. Falcovitz, Generalized Riemann Problems in Computational Fluids Dynamics, Cambridge University Press, 2003.
[8] D.J. Benson, Computational methods in Lagrangian and Eulerian hydrocodes, Comput. Methods Appl. Mech. Eng. 99 (1992) 235–394.
[9] J. Botsis, M. Deville, Mécanique des milieux continus: une introduction, Presses Polytechniques et Universitaires Romandes, Lausanne, 2006.
[10] A.F. Bower, Applied Mechanics of Solids, CRC Press, Boca Raton, 2009.
[11] E.J. Caramana, D.E. Burton, M.J. Shashkov, P.P. Whalen, The construction of compatible hydrodynamics algorithms utilizing conservation of total energy, J. Comput. Phys. 146 (1998) 227–262.
[12] B. Després, C. Mazeran, Lagrangian gas dynamics in two dimensions and Lagrangian systems, Arch. Rational Mech. Anal. 178 (2005) 327–372.
[13] J. Donea, A. Huerta, J.-Ph. Ponthot, A. Rodriguez-Ferran, Encyclopedia of Computational Mechanics, volume 1: Fundamentals, Chapter 14: Arbitrary Lagrangian–Eulerian Methods, John Wiley and Sons, 2004.
[14] J.K. Dukowicz, A general non-iterative Riemann solver for Godunov's method, J. Comput. Phys. 61 (1984) 119–137.
[15] J.K. Dukowicz, M.C. Cline, F.S. Addessio, A general topology method, J. Comput. Phys. 82 (1989) 29–63.
[16] V. Dyadechko, M. Shashkov, Reconstruction of multi-material interface from moment data, J. Comput. Phys. 227 (11) (2008) 5361–5384.
[17] D. Eberly, Triangulation by ear clipping, Geometric Tools, LLC, 2008. Available at: <http://www.geometrictools.com/Documentation/TriangulationByEarClipping.pdf>.
[18] S. Galera, M. Kucharik, P.-H. Maire, M. Shashkov, M. Berndt, J. Breil, Hybrid remapping (conservative interpolation) for multimaterial arbitrary Lagrangian–Eulerian methods, J. Comput. Phys., submitted for publication.
[19] J. Glimm, J.W. Grove, X.L. Li, W. Oh, D.H. Sharp, A critical analysis of Rayleigh–Taylor growth rates, J. Comput. Phys. 169 (2001) 652–677.
[20] J. Glimm, J.W. Grove, X.L. Li, K.M. Shyue, Q. Zhang, Y. Zeng, Three dimensional front tracking, SIAM J. Sci. Comput. 19 (1998) 703–727.
[21] J.F. Haas, B. Sturtevant, Interaction of weak-shock waves, J. Fluid Mech. 181 (1987) 41–76.
[22] C.W. Hirt, A. Amsden, J.L. Cook, An arbitrary Lagrangian–Eulerian computing method for all flow speeds, J. Comput. Phys. 4 (1974) 227–253.
[23] P. Hoch, An arbitrary Lagrangian–Eulerian strategy to solve compressible fluid flows, HAL: hal-00366858, version 1, 2009. Available at: <http://hal.archives-ouvertes.fr/docs/00/36/68/58/PDF/ale2d.pdf>.
[24] J.R. Kamm, M. Shashkov, A pressure relaxation closure model for one-dimensional, two-material Lagrangian hydrodynamics based one the Riemann problem, Technical Report LA-UR-09-00659, Los Alamos National Laboratory, 2009.
[25] J.R. Kamm, F.X. Timmes, On efficient generation of numerically robust Sedov solutions, Technical Report LA-UR-07-2849, Los Alamos National Laboratory, 2007.
[26] P. Knupp, Achieving finite element mesh quality via optimization of the Jacobian matrix norm and associated quantities. Part I – A framework for surface mesh optimization, Int. J. Numer. Methods Eng. 48 (2000) 401–420.
[27] P. Knupp, Algebraic mesh quality metrics, SIAM J. Sci. Comput. 23 (1) (2001) 193–218.
[28] P. Knupp, L.G. Margolin, M.J. Shashkov, Reference Jacobian optimization-based rezone strategies for arbitrary Lagrangian–Eulerian methods, J. Comput. Phys. 176 (2002) 93–128.
[29] P. Knupp, S. Steinberg, Fundamentals of Grid Generation, CRC Press, Boca Raton, 1993.
[30] P.M. Knupp, Achieving finite element mesh quality via optimization of the Jacobian matrix norm and associated quantities. Part I – A framework for surface mesh optimization, Int. J. Numer. Methods Eng. 48 (3) (2000) 401–420.
[31] M. Kucharik, R.V. Garimella, S.P. Schofield, M.J. Shashkov, A comparative study of interface reconstruction methods for multi-material ale simulations, J. Comput. Phys. 229 (7) (2009) 2432–2452.
[32] M. Kucharik, M. Shashkov, Extension of efficient, swept-integration-based conservative remapping method for meshes with changing connectivity, Int. J. Numer. Methods Fluids 56 (8) (2008) 1359–1365.
[33] J.D. Lindl, Inertial Confinement Fusion, Springer, 1998.
[34] R. Loubère, P.-H. Maire, M. Shashkov, J. Breil, S. Galera, Reale: A Reconnection-based Arbitrary Lagrangian–Eulerian Method, Technical Report LA-UR-09-07844, Los Alamos National Laboratory, 2009.

[35] R. Loubère, P.-H. Maire, M. Shashkov, J. Breil, S. Galera, Reale: a reconnection-based arbitrary Lagrangian–Eulerian method, J. Comput. Phys. 229 (2010) 4724–4761.
[36] H. Luo, J.D. Baum, R. Löhner, On the computation of multi-material flows using ALE formulation, J. Comput. Phys. 194 (2004) 304–328.
[37] P.-H. Maire, A high-order cell-centered Lagrangian scheme for two-dimensional compressible fluid flows on unstructured meshes, J. Comput. Phys. 228 (2009) 2391–2425.
[38] P.-H. Maire, R. Abgrall, J. Breil, J. Ovadia, A cell-centered Lagrangian scheme for compressible flow problems, SIAM J. Sci. Comput. 29 (4) (2007) 1781–1824.
[39] P.-H. Maire, J. Breil, S. Galera, A cell-centered arbitrary Lagrangian–Eulerian (ALE) method, Int. J. Numer. Methods Fluids 56 (2008) 1161–1166.
[40] L.G. Margolin, Introduction to "An arbitrary Lagrangian–Eulerian computing method for all flow speeds", J. Comput. Phys. 135 (2) (1997) 198–202.
[41] L.G. Margolin, M. Shashkov, Second-order sign-preserving remapping on general grids, J. Comput. Phys. 184 (2003) 266–298.
[42] B. Mirtich, Fast and accurate computation of polygonal mass properties, J. Graphics Tools 1 (1996) 31–50.
[43] J.M. Morrell, P.K. Sweby, A. Barlow, A cell by cell anisotropic adaptive mesh ALE scheme for the numerical solution of the Euler equations, J. Comput. Phys. (2007) 1152–1180.
[44] B. Nkonga, On the conservative and accurate CFD approximations for moving meshes and moving boundaries, Comput. Methods Appl. Mech. Eng. 190 (13-14) (2000) 1801–1825.
[45] James J. Quirk, S. Karni, On the dynamics of a shock-bubble interaction, J. Fluid Mech. 318 (1996) 129–163.
[46] B. Rebourcet, ModTlisations numTriques multifluides et multiphases – liens de principe, Technical Report DO 119, CEA, 2006.
[47] M. Shashkov, Closure models for multimaterial cells in arbitrary Lagrangian–Eulerian hydrocodes, Int. J. Numer. Methods Fluids 56 (2008) 1497–1504.
[48] P. Vachal, R.V. Garimella, M.J. Shashkov, Untangling of 2D meshes in ALE simulations, J. Comput. Phys. 196 (2004) 627–644.
[49] A.M. Winslow, Equipotential Zoning of Two-Dimensional Meshes, Technical Report UCRL-7312, Lawrence Livermore National Laboratory, 1963.
[50] A.M. Winslow, Numerical solution of the quasilinear poisson equation in a nonuniform triangle mesh, J. Comput. Phys. 1 (2) (1966) 149–172. Reprinted in 135(2) (1997) 128–138.
[51] D.L. Youngs, Time dependent multi-material flow with large fluid distortion, in: K.W. Morton, M.J. Baines (Eds.), Numerical Methods for Fluid Dynamics, Academic Press, New York, 1982, pp. 273–285.
[52] D.L. Youngs, Multi-mode implosion in cylindrical 3d geometry, in: 11th International Workshop on the Physics of Compressible Turbulent Mixing (IWPCTM11), Santa Fe, 2008.